THE STORAGE RING FREE-ELECTRON LASER

R.J. Bakker[1]
CEA/DSM/DRECAM/SPAM, Cen-Saclay, France
LURE, Orsay, France

Abstract
In a storage-ring free-electron laser (SRFEL) the circulating current of a ring forms the driver for the free-electron laser. The storage ring provides excellent beam parameters and it seems an ideal candidate for a tuneable laser for the ultra-violet and vacuum ultraviolet spectral range. At present experiments demonstrate stable operation with good spectral properties in the UV spectral range, i.e. down to a wavelength of 240 nm. Construction of such a device is non-trivial, however, and optimisation of both the laser and the storage ring is necessary. The SRFEL also has a more complex dynamic behaviour as compared to linac-driven FEL's since the dynamics of both the laser and the storage ring are involved. Here follows a discussion of both the design and the operational aspects of this device.

1. INTRODUCTION

The storage ring free-electron laser (SRFEL) employs the circulating current in a storage ring to drive the gain of the laser. Figure 1 shows the fundamental layout of such a device. An undulator is located in a dispersion-free section of the ring. Next, the synchrotron radiation is captured in a resonator to enable the interaction between the electrons and the optical field. As a FEL driver, the storage-ring has excellent beam parameters, e.g., a low energy spread and a low emittance. Because of the typical beam-energy of rings, the laser is specially suited for operation at short wavelengths (< 700 nm). Difficulties with optics will, most probably, limit the use to the vacuum ultra-violet (VUV) spectral range.

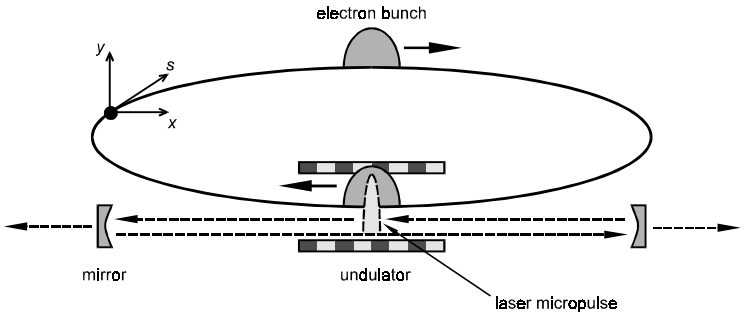

Fig. 1 Schematic layout of the Storage Ring Free Electron Laser (SRFEL). The radiation that is produced by the circulating electrons in the storage-ring passing through an undulator is captured between two mirrors. Due to the interaction between the circulating electron bunches and the stored optical pulse, the characteristic FEL process can take place. The example sketched is typical for a two-bunch mode of operation, i.e. two bunches in the storage ring that both interact with one optical pulse in the resonator.

---

1 Correspondence address: Berliner Elektronenspeicherring Gesellschaft für Synchrotronstrahlung mbH, Lentzeallee 100, D-14195 Berlin, Germany

The first operation of a storage-ring based FEL was demonstrated at a wavelength of 650 nm on ACO in Orsay, France in 1983 [1]. Since then the field has become maturer and on several rings such as VEPP-3 (Novosibirsk, Russia) [2], UVSOR (Okazaki, Japan) [3] and Super ACO (Orsay, France) [4] the FEL process has been studied. New challenging projects are starting, or close to, operation, e.g. at Duke University (Durham, USA) [5] and DELTA (Dortmund, Germany) [6]. A more complete overview is given in Table 1. Recent developments also demonstrated the feasibility of the SRFEL as a light source for user experiments. For example at Super ACO where up to 50% of the FEL beam-time is used to facilitate user experiments [11]. The SRFEL has the advantage that it is naturally synchronised with the additional beam lines along the ring. One thus has two synchronised high-brilliance polarised light sources with tuneable wavelength in the UV or VUV. The SRFEL forms an ideal tool for pump-probe experiments with a high repetition rate. For example at Super ACO such experiments are performed with a repetition rate of 8.3 MHz. Here the FEL either serves as pump or as probe [11].

Table 1

Storage-ring free-electron laser facilities

Project	**Location**	**Ref.**	**Status**[1)]	*E* [GeV]	λ [nm]	**Gain** [%]	**Remarks**
ACO	France, Orsay	[1]	a	0.16-0.25	460-650	0.4	First SRFEL
DELTA	Germany, Dortmund	[6]	c	0.5-1.5	100-400		Dedicated
Duke Univ.	USA, Durham	[5]	o	1	25-400		Dedicated
KEK	Japan, Tsukuba	[7]	c	0.75	170-220		
NIJI-IV	Japan, Tsukuba	[8]	o	0.24	350	2.3	Dedicated
Soleil	France	[9]	p	1.5	100-350		Synchrotron
Super ACO	France, Orsay	[4]	o	0.6-0.8	350-600	2.5	Synchrotron
TERAS	Japan, Tsukuba	[10]	a	0.24	598	> 0.1	
UVSOR	Japan, Okazaki	[3]	o	0.5	290-500		
VEPP-3	Russia, Novosibirsk	[2]	a	0.35-0.5	240-690	10.0	Nucl. phys.

[1)] a - abandoned, c - construction, o - operational, p - proposed

In the SRFEL the beam in the storage ring serves as a source for the FEL interaction. Apart from this the SRFEL is not fundamentally different from other types of free-electron lasers. Hence, all aspects that are of importance for a (linac driven) FEL are similarly important in the SRFEL. The storage ring has several properties that make it a good choice as a driver. In a modern ring it is possible to obtain a high current in combination with an excellent beam quality, for example, a stable beam with a low energy-spread, a small emittance, and a high peak current. It is important to note that in a storage ring the beam is recirculated. This gives the storage ring the advantages of 100% duty cycle (the beam runs continuously for many hours). Because of limitations to the rf power needed, conventional linacs generally operate with macro pulses with a duty cycle less than one percent. The recirculation also causes a coupling between the dynamics of the laser and ring. This makes the storage ring a different and a more complex beam source. Consequently the performance, characteristics and dynamic behaviour of the SRFEL are different from FEL's using other types of accelerators. The achievable output-power of the SRFEL is, for example, different from one driven by a linear accelerator. In the storage ring the recirculation limits the achievable peak-power. The peak-power of an SRFEL is therefore lower than the peak-power of a linac driven FEL. Because of its 100 % duty cycle the average power level is much higher, however. Typical values are depicted in Figs. 2 and 3.

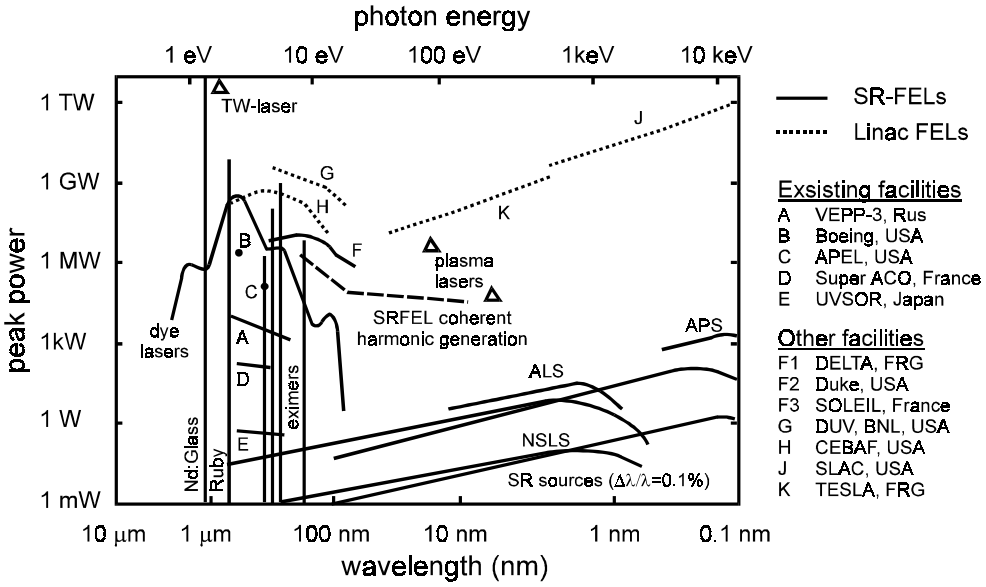

Fig. 2 Overview of achieved and predicted peak powers for several synchrotron and FEL light-sources [12]. See Table 1 for references to the SRFEL light-sources.

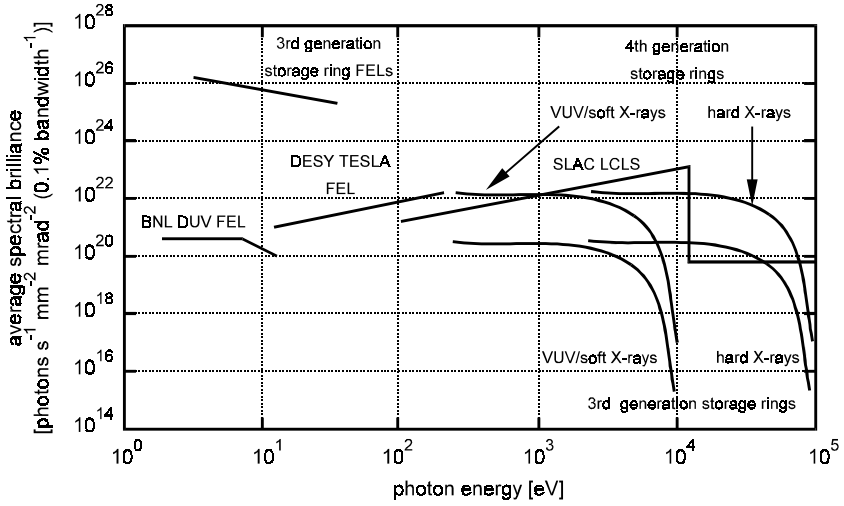

Fig. 3 Achieved and predicted average spectral brightness of several synchrotron and FEL light-sources [13]. See Table 1 for references to the SRFEL light-sources.

The performance of the linac-based and the ring-based FEL's are different by other factors as well. The laser micropulse length in the linac is typically shorter than that of the ring system, i.e. down to a sub-pico-second level in a linac versus several tens of pico-seconds for a ring. It is expected that the achievable peak current and, hence, the laser gain, of a linac-based system can be much higher. As a result the linac based FEL is a better-suited candidate for a single-pass mode of operation where spontaneous emission will be amplified to saturation in a single-pass (SASE - Self-Amplified Spontaneous Emission). This is especially important for short-wavelength operation where presently no mirror material is available for resonators, i.e. wavelengths less than 50 nm. In terms of stability and the quality (e.g. spectral width) of the emitted radiation, it is more advantageous to use a resonator. Due to this and the fact that the beam can be more stable in a ring, the SRFEL is a better candidate for stable user

source at wavelengths where optics are available. Furthermore, unlike the alternative, the SRFEL already has a record of obtained results. An overview is given in Table 2. It is expected that several of these parameters will be improved soon since two new lasers at Duke University and at Dortmund University are close to being operational. Both machines have the novel feature that the storage ring has been specially optimised for FEL operation. Hence, their performance, in terms of the small-signal gain and the expected output power, are expected to overshadow the performance of the presently operational SRFEL's.

Table 2

Experimental results obtained

Shortest wavelength:	λ_{min}	240	nm	VEPP-3
		239	nm	UVSOR
Rms minimum line-width:	$\Delta\lambda/\lambda$	$3\cdot10^{-7}$		VEPP-3
Maximum small-signal gain:	G	10	%	VEPP-3
Maximum peak power:	P_{max}	60	kW	VEPP-3
Maximum average power:	P_a	100	mW	Super ACO
Maximum duration of CW operation:	T	10	hours	Super ACO

The contents of this chapter can be divided into two parts. Sections 2 and 3 describe the process of gain and saturation in the SRFEL while sections 4 and 5 discuss the essential parts for the design of a storage-ring FEL: the resonator and the optimisation of the ring. Additionally there are two appendices. The major parts of the experimental examples of laser operation are obtained from the Super ACO FEL experiment. For reference Appendix A gives an overview of this machine and some of its diagnostic equipment. Appendix B presents the details of a gain model that is used in the calculations presented in Sections 2, 4 and 5.

2. THE FEL GAIN

The SRFEL is generally a low-gain device. That is, the laser saturates after the light has passed many times through the undulator. For such a laser to operate, the gain must initially exceed the threshold losses. Hence, the single-pass small-signal gain is an important parameter. Quantitative analyses of the FEL gain are given in Appendix B. It is often useful to start with a more qualitative description. The Madey theorem [14] states that the single-pass small-signal FEL gain is proportional to the derivative of the spontaneous emission spectrum. It thus follows that any modification of the spontaneous emission spectrum of the undulator can be translated into a change in the small-signal gain. Experimentally this is an important aspect since it is often easy to measure the spontaneous emission of an undulator. The spontaneous emission can, therefore, serve as a tool to optimise the FEL gain.

A quantitative prediction of the small-signal gain for a planar undulator shows that in a storage ring the regular planar undulator is not an optimum choice. More gain can be obtained through a modification of the undulator into a so-called Optical Klystron (OK). A description and quantitative analyses of this device is given in Section 2.3.

2.1 The Madey theorem

The physics behind the Madey theorem is best explained in the so-called rest frame of the electrons, i.e. the coordinate system in which the net forward velocity of the electrons is zero. This frame is illustrated in Fig. 4. Photons originating from the optical field move from

the left to the right. Virtual undulator photons move in the opposite direction. In the rest frame both emission and absorption can be described as Compton scattering. In the case of emission a virtual undulator photon, moving in backward direction with energy $\hbar\omega_u'$ transforms into a light photon $\hbar\omega_e'$ with forward velocity due to scattering. Here $\hbar$ denotes Planck's constant divided by 2π. The prime indicates that the frequencies are related to the rest frame. In case of absorption the opposite process results in the transformation of a light photon $\hbar\omega_a'$ into a virtual undulator photon $\hbar\omega_u'$. In the laboratory frame, i.e. the frame of the observer, the corresponding wavelength transforms back into the well-known relation of the fundamental wavelength of the undulator radiation λ:

$$\lambda = \frac{\lambda_u}{2\gamma^2}\left(1 + \frac{K^2}{2} + \gamma^2\theta^2\right)$$
$$K = \frac{eB_u\lambda_u}{2\pi mc} \qquad (1)$$

where λ_u, γ, θ denote the undulator period, the Lorentz factor corresponding to the beam energy ($\gamma \approx E$ [MeV]/0.511), and the angle between the forward propagation direction of the electron beam with respect to the magnetic axis of the undulator, respectively. The magnetic field-strength of the undulator is transformed into the dimensionless parameter K in which B_u denotes the peak magnetic field strength on axis.

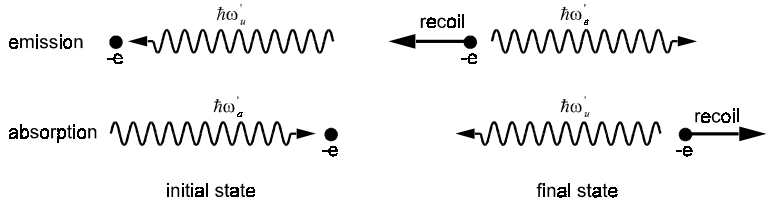

Fig. 4 Scattering interaction for a single electron in the rest frame. In the figure $\hbar\omega_u'$, $\hbar\omega_e'$, and $\hbar\omega_a'$ denote the virtual undulator photon, the emitted photon and the absorbed photon, respectively. The prime indicates that all frequencies are in the rest frame.

By the definition of the rest frame the net electron velocity is zero. Hence, the scattering process always increases the kinetic energy of an electron due to recoil, both in the case of absorption and emission. Because of energy conservation, the energy contained by a scattered photon is always less than the energy of the original photon. Hence, $\hbar\omega_u' > \hbar\omega_e'$ in the case of emission and $\hbar\omega_a' > \hbar\omega_u'$ for absorption. Since the frequency of the virtual undulator photon is related to the definition of the rest frame, i.e. see Eq. (1), it follows that the energy of the electron beam must increase in order to emit a photon with the same frequency. Similarly the electron beam energy must decrease in order to absorb a photon at the central frequency ω_s'. Hence, emission and absorption of a photon with energy $\hbar\omega_s'$ require different electron beam energies. This is illustrated in Fig. 5a. A quantitative value for the shift, $\Delta\gamma$, depends on the magnitude of the electron recoil. The derivative of the spontaneous emission spectrum, therefore, maps to the gain spectrum, see Fig. 5b. Electrons injected into the FEL slightly above the resonant energy contribute to net stimulated emission. Electrons injected at a slightly too low energy give rise to net absorption. In the former case the working of the FEL is reversed and it operates as an electron accelerator.

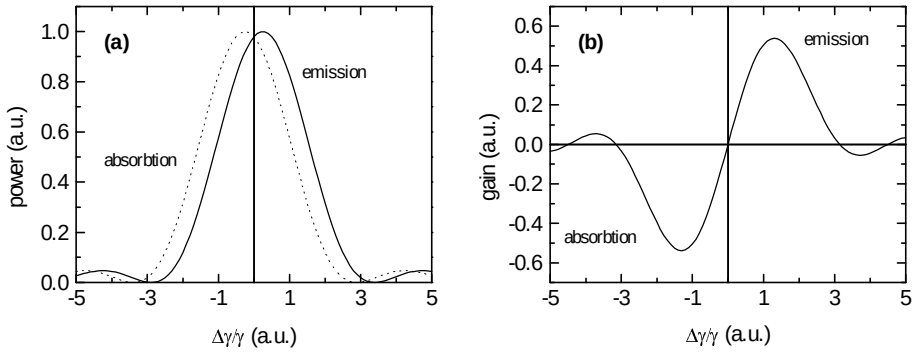

Fig. 5 Emission and absorption spectrum of an electron pass through a two-wave FEL (a) and the resulting gain spectrum (b).

2.2 The FEL gain for a planar undulator

This text follows the gain calculations made by Dattoli et al. [15]. The peak single-pass gain for a perfect one-dimensional electron beam, i.e. no energy spread and infinitely small transverse beam-size, can be found to be

$$G_0 = 0.27\,\pi\, g_0 \tag{2}$$

where g_0 is the so-called gain parameter which for a planer undulator and low gain ($g_0 < 1$) is given by

$$g_0 = 2\pi \frac{J}{I_A} K^2 N^3 \frac{\lambda_u^2}{\gamma^3} JJ \tag{3}$$

where J, I_A, and N denote the electron current density, the Alfvén current (≈17 kA), and the number of undulator periods, respectively. The parameter JJ

$$\begin{aligned} JJ &= \left(J_0(\xi) - J_1(\xi)\right)^2 \\ \xi &= \frac{K^2}{4 + 2K^2} \end{aligned} \tag{4}$$

accounts for the gain reduction due to the periodic detuning of the electrons in a planar undulator (see Ref. [16] p. 73), where J_0 and J_1 are Bessel functions of the first kind.

The transverse overlap of the electron beam and the EM wave is usually taken into account by multiplication of the gain parameter with a heuristic filling factor, for a narrow electron beam defined as the ratio of the transverse cross section of the electron beam and the EM wave. Under the assumption of a diffraction-limited Gaussian beam, the average transverse cross section of the EM wave along the undulator is proportional to the undulator length $N\lambda_u$, and the wavelength λ, see Section 4.1. For an optimum overlap the filling factor, F, is found to be [17]

$$F = \frac{3}{2} \frac{\Sigma_e}{N\lambda_u\,\lambda} \tag{5}$$

where the transverse cross section of the electron beam, averaged along the undulator, is denoted as Σ_e. Substitution of the Eqs.(5), (3) and (1) into Eq. (2) leads to

$$G_0 = 3.76 \cdot 10^{-3} N^2 I(A) \frac{\xi}{\gamma} JJ \tag{6}$$

where I also substituted the beam current, $I = J\Sigma_e$. It should be realised that this gain formula is only valid for 'ideal', continuous electron beams, i.e. for continuous-wave (cw) beams with negligible energy spread and emittance. This assumption is certainly not correct for a realistic beam and G_0 needs to be corrected.

First, the influence of the finite beam emittance is discussed, i.e. the influence of the finite beam radius and divergence. Due to the fact that the magnetic field has a sinusoidal z-dependence on the axis of the undulator, off-axis electrons experience a slightly different field (because $\nabla \cdot \mathbf{B} = 0$), and thus also a slightly different K that leads to a different wavelength than is given by Eq. (1). Also, electrons moving under a small angle θ give rise to a different wavelength. It can be calculated that this leads to the following emittance-induced inhomogeneous broadening of the line-width [15]:

$$\left(\frac{\Delta\omega}{\omega}\right)_{x,y} = \frac{2\gamma^2}{1+\frac{K^2}{2}} \sqrt{\frac{1}{2}\sigma_{x',y'}^4 + \frac{1}{2}\left(\frac{\pi K}{\gamma\lambda_u}\right)^4 h_{x,y}^2 \sigma_{x,y}^4} \tag{7}$$

where σ_x and σ_y denote the standard deviation of the particle distribution in the x- and y-direction respectively; the wiggle motion takes place in the *x-z* plane. Further, $\sigma_{x'}$ and $\sigma_{y'}$ denote the standard deviation of the corresponding transverse velocity distributions. The parameter h denotes the sextupole term of the undulator, i.e. $h_x = h_y = 0$ for a helical undulator and $h_x \approx 0$, $h_y \approx 2$ for a planar undulator. The parameters $\sigma_{x,y}$ and $\sigma_{x',y'}$ are coupled through the unnormalized beam emittance $\varepsilon_{x,y}$. In the case of a 100 % coupled cylindrical beam, i.e. $\varepsilon = \varepsilon_x = \varepsilon_y$ and $\sigma_x = \sigma_y$, it is found that the gain-reduction due to the finite emittance can be expressed as [15]:

$$\begin{aligned} C_{x,y} &= \frac{1}{1+\mu_{x,y}^2} \\ \mu_x &= \pi N \sqrt{2} \frac{\gamma\varepsilon}{\lambda_u} \frac{K^2}{4+2K^2} \\ \mu_y &= 2\pi N \frac{\gamma\varepsilon}{\lambda_u} \frac{K^2}{4+2K^2} \end{aligned} \tag{8}$$

where $\mu_{x,y}$ expresses the relative broadening of the spontaneous emission spectrum, i.e. $\mu_{x,y} = (\Delta\omega/\omega)_{x,y} / (\Delta\omega/\omega)_0$. The corrections are valid up to (at least) $\mu_{x,y} = 1$.

Also important is the influence of a finite energy spread. It follows from Eq. (1) that the spectrum of spontaneous emission broadens in the case of non-zero electron-beam energy spread and, the gain is reduced (Madey theorem). A quantitative estimate of the gain-reduction is found to be [15]:

$$\begin{aligned} C_e &= \frac{1}{1+1.7\mu_e^2} \\ \mu_e &= \frac{1}{4N(\sigma_\gamma/\gamma)} \end{aligned} \tag{9}$$

where σ_γ denotes the standard deviation associated with the energy distribution. Eq. (9) is valid for $\mu_e \leq 2$. Substitution of Eq. (8) and Eq. (9) into Eq. (2) leads to:

$$G_0 = 3.76 \cdot 10^{-3} N^2 I C_e C_x C_y \frac{\xi}{\gamma} JJ . \tag{10}$$

From Eq. (9) it follows that the influence of energy spread, and hence the gain reduction due to the energy-spread, increases as the number of undulator periods increases. However, the maximum gain also increases, see Eq. (10). It is thus possible to calculate an optimum undulator length:

$$L_{opt} = \frac{\lambda_u}{2(\sigma_\gamma / \gamma)} . \tag{11}$$

In storage rings the energy spread is generally low and, hence, the optimum undulator length can be considerable. As a result the optimum undulator length is normally much more than the length of the straight sections. For example at Super ACO (λ_u=12.9 cm, $\sigma_\gamma/\gamma=0.65\times10^{-3}$) it follows that L_{opt} = 99 m. The available space in the straight section is less than 4 m, however. This dilemma can be solved through a modification of the undulator.

2.3 The Optical Klystron

The Optical Klystron is a modified version of the undulator that was originally proposed to improve the gain of an FEL with a limited straight section length and small energy spread [18], for example, the SRFEL. The OK consists of a set of two undulators separated by a dispersive section, see Fig. 6. The first undulator serves as a modulator, i.e. due to the interaction with the optical field, the electron beam energy is modulated *on the scale of the fundamental wavelength.* In the dispersive section, low-energy electrons are retarded with respect to the high-energy electrons. Hence, the energy-modulation is transformed into a longitudinal modulation (micro bunching). As a result the coherent radiation and gain in the second undulator is enhanced. The main advantage of an OK is the gain enhancement for a given interaction length. The saturated power level is reduced, however.

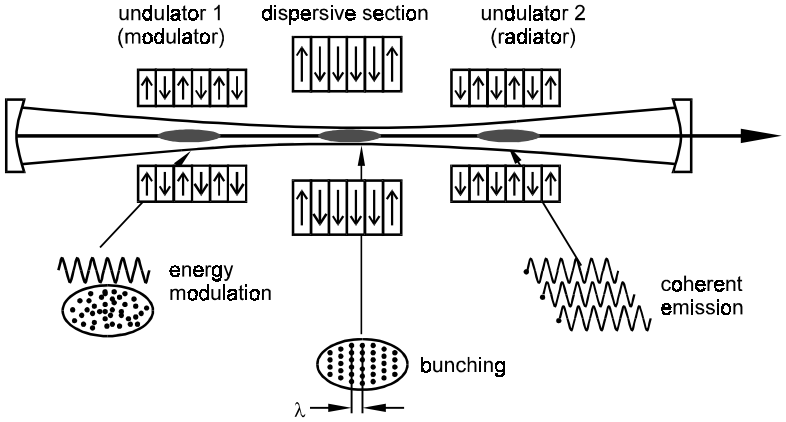

Fig. 6 Schematic diagram of a transverse optical klystron

Insight into the magnitude of the gain enhancement can be deduced from the spontaneous-emission power-spectrum of the OK which serves as a delay between the electrons and the optical wavefront. Consequently the spontaneous emission of both undulators interfere similarly to the interference between two slits. The total radiated intensity I_{OK} can be written as [19]:

$$I_{OK} = 2I_0\left(1+\cos\delta\right) \tag{12}$$

where I_0 denotes the intensity of the spontaneous radiation of a single undulator section. The phase delay δ b etween the entrance of the two undulators has to be separated into two components: the delay in the first undulator section (slippage = $N\lambda$) and that in the dispersive section.

$$\delta = 2\pi(N+N_d)\frac{\Delta\lambda}{\lambda_R} \tag{13}$$

Here λ_R is the resonant wavelength defined in Eq. (1). The new parameter N_d defines the number of wavelengths over which the electrons are delayed in the dispersive section, relative to the optical wavefront. For a standard magnetic dispersive section this can be written as [20]:

$$N_d = \frac{L_d}{2\gamma^2\lambda}\left[1+\frac{1}{L_d}\left(\frac{e}{mc}\right)^2\int_0^{L_d}\left(\int_0^u B(z)\mathrm{d}z\right)^2\mathrm{d}u\right] \tag{14}$$

where *B(z)* denotes the transverse magnetic field and L_d the length of the dispersive section respectively. An example of the spontaneous emission spectrum of the optical klystron is given in Fig. 7. The ideal case is depicted in Fig. 7a, i.e. the spectrum that one can expect from an ideal electron beam traversing an ideal optical klystron. From the steeper slopes of the spectrum it follows that the gain is significantly enhanced. Generally the spectrum is deteriorated, however, and the modulation depth *f* defined as

$$f = \frac{I_{\max}-I_{\min}}{I_{\max}+I_{\min}} \tag{15}$$

is reduced, see Fig. 7b. Here the reduction of the modulation depth due to a finite energy spread is the most important. For a Gaussian distribution it can be derived that [20]:

$$f = e^{-2\left(2\pi(N+N_d)\frac{\sigma_\gamma}{\gamma}\frac{\lambda}{\lambda_R}\right)^2}. \tag{16}$$

The gain for an OK is found to be [21]:

$$G_{ok} = 0.93\frac{G_0(2N)}{N}(N+N_d)\,f\,C_f \tag{17}$$

where G_0 is the homogeneous gain as defined in Eq. (2). The parameter C_f is used to compensate for the transverse overlap between the electron beam and the optical beam. In the case of a Gaussian transverse electron distribution and a TEM_{00} resonator mode a good estimate can be obtained by [20]:

$$C_f = \frac{2}{\sqrt{4\sigma_x^2+w_0^2}}\frac{2}{\sqrt{4\sigma_y^2+w_0^2}} \tag{18}$$

where additional to the previous definition, w_0 is the waist size of the optical field in the resonator (see Sec. 3). From Eq. (16) it can be found that the optimum value, i.e. the maximum gain is obtained when [21]:

$$N + N_d = \frac{1}{4\left(\sigma_\gamma / \gamma\right)}. \tag{19}$$

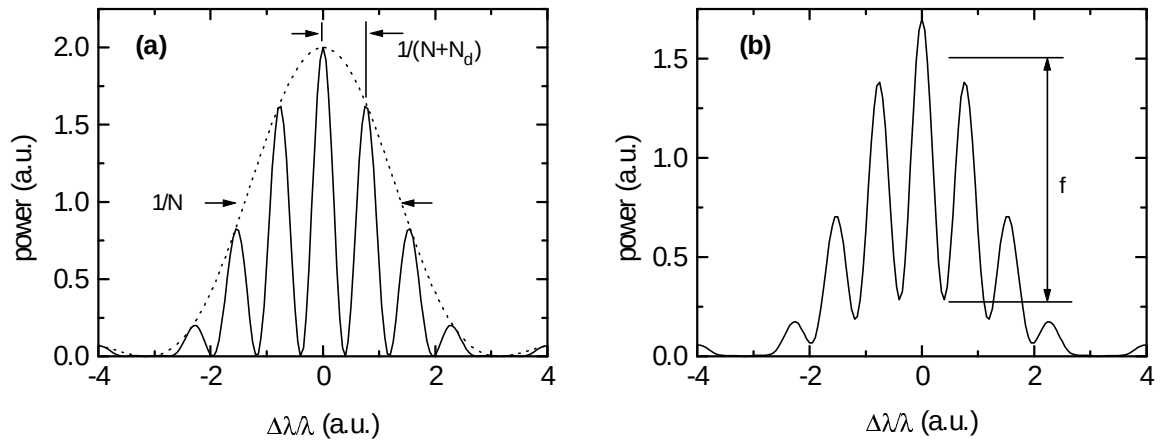

Fig. 7 Spontaneous emission spectrum of an optical klystron: (a) homogeneous spectrum and (b) deteriorated spectrum due to inhomogeneous effects.

An experimental example of the gain enhancement of an OK is shown in Fig. 8. Figure 8a is the measured spectrum of the OK used in the Super ACO FEL (solid line). The corresponding spectrum of this device used as a regular undulator, i.e. $N_d = 0$, is depicted as a dashed line. The gain curve shown in Fig. 8b is obtained using the derivative of the spectrum shown in Fig. 8a (Madey's theorem). The gain enhancement obtained is clearly visible.

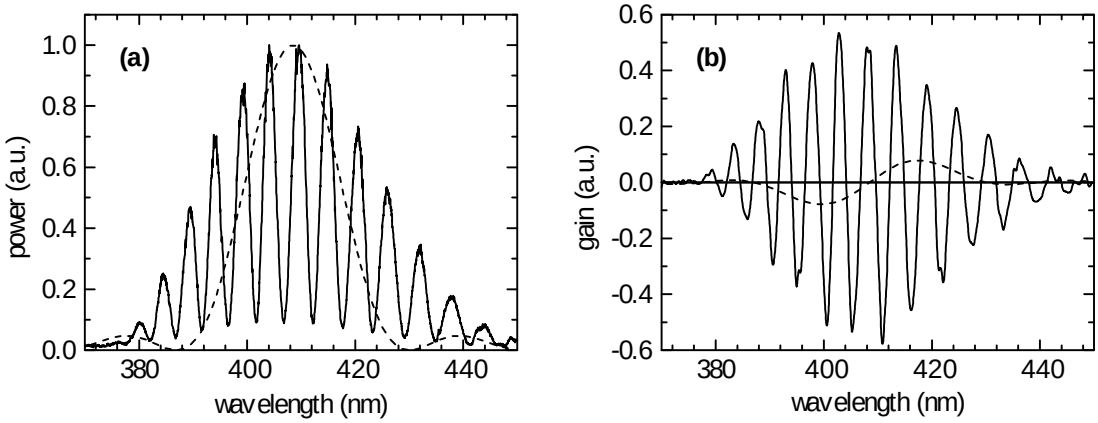

Fig. 8 The spontaneous emission spectrum (a) and the derived small signal gain (b) measured with the Super ACO optical klystron SU7 (solid line). The dashed line corresponds to the spontaneous emission spectrum and gain of an undulator with similar length as the OK, i.e. 2*N* periods.

3. SATURATION

The saturation mechanism of an SRFEL is fundamentally different from a linac driven FEL. In a linac-driven FEL the electron beam is dumped after it has passed through the undulator. In a storage-ring free-electron laser the electron beam is recirculated. Hence, any

perturbation of the electron beam due to the FEL interaction is coupled back to the laser on the next pass through the undulator. Initially this effect is small since, in the small signal case, there is virtually no perturbation of the electron beam. As the optical power grows more energy is extracted from the electron beam and the energy spread increases. This causes a decrease in FEL gain for a multiple of reasons. Firstly because of inhomogeneous broadening of the small-signal gain profile: see Eqs. (9) and (19). Secondly the increase in energy spread can cause bunch lengthening. In a storage ring the bunch length and the energy spread are coupled through the so-called momentum-compaction factor [22]:

$$\alpha \approx \frac{\Delta L / L}{\Delta E / E} \tag{20}$$

which expresses the path lengthening ΔL of a particle with an energy difference ΔE, relative to the reference energy E and the circumference of the storage ring L. The change in bunch duration σ_t depends on both α and the angular synchrotron oscillation frequency ω_s [23]

$$\sigma_t = \frac{\alpha}{\omega_s}\frac{\sigma_\gamma}{\gamma}. \tag{21}$$

Bunch lengthening automatically translates into a reduction of the peak current and, hence, the gain. Finally this leads to an equilibrium state where the small-signal gain is reduced to the cavity losses. The saturation process is schematically depicted in Fig. 9. The left-hand side (a) shows that the gain drops as the optical power increases. On the right-and side (b) the evolution of the gain and the energy spread is plotted.

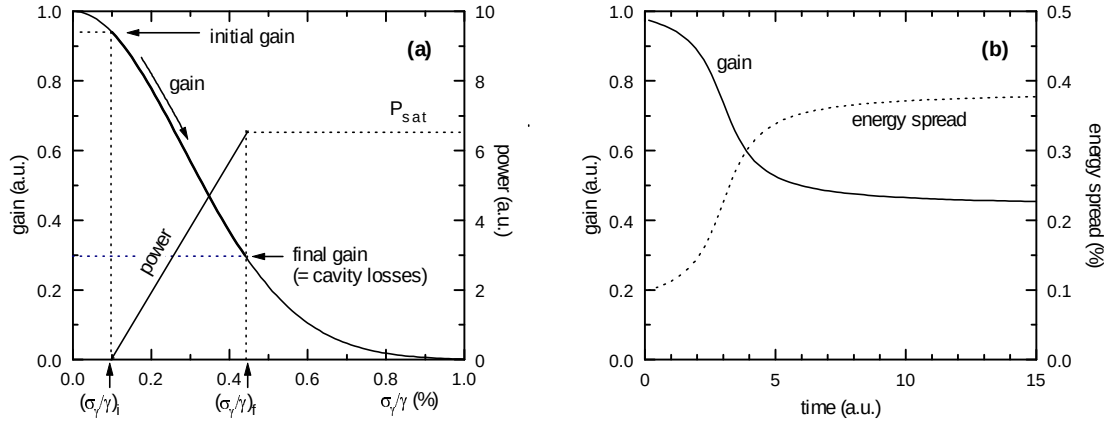

Fig. 9 The saturation process of the SRFEL: as the optical power increases the FEL gain drops (a) due to a decrease in gain induced by an increased energy spread (b).

The magnitude of the extracted power and the induced energy spread depend on the design of both the FEL and the storage ring. For example, an optical klystron with a high value for $N+N_d$ has a higher initial gain but is more sensitive to an increase in energy spread, see Eq. (19). Hence, with a high value for $N+N_d$ the laser power grows more quickly but saturates at a lower level. Simultaneously the induced energy spread at saturation is reduced.

An experimental example taken from the UVSOR FEL is depicted in Fig. 10 [24]. It shows the evolution of the laser power measured simultaneously with the electron bunch length in the ring. The origin of the horizontal axis corresponds with the moment at which the laser is switched “on”. That is, the electron beam parameters are tuned such that the gain

exceeds the cavity losses. During the increase of power the electron bunch becomes longer and the peak current decreases and, hence, the gain decreases. As the gain drops below threshold the optical power decreases.

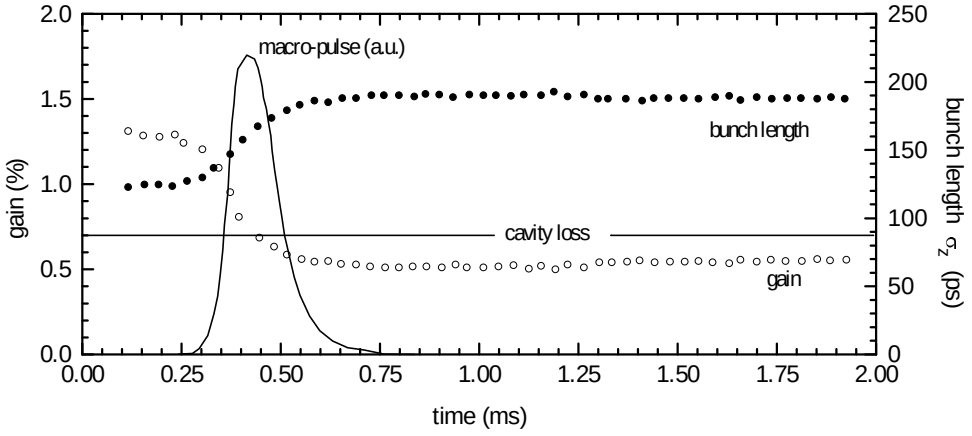

Fig.10 Evolution of the bunch length and the gain in a Q-switched mode. The bunch length has been measured with a dual-sweep streak camera. The gain is derived from the bunch length. The solid line shows the macropulse measured with a photo-diode [24]. The streak camera is described in Appendix A.

From Fig. 10 it follows that the actual saturation process is much more complicated than the situation depicted in Fig. 9. For a better understanding both the dynamics of the FEL and the storage ring need to be considered. Most important here is the damping of induced energy spread in the storage ring. Generally the power, gain and energy spread do not evolve as smoothly as depicted in Fig. 9. The following sub-sections discuss a quantitative description of the steady-sate parameters (Sec. 3.1 and 3.2) and the dynamic properties (Sec. 3.3 to 3.5).

3.1 The Average Output Power

The average output power of the SRFEL was first studied by Renieri [25] who solved the Fokker-Plank equation for the electron-distribution in the presence of the FEL. He found that the average output power is limited to a small fraction of the synchrotron power emitted all around the ring (P_{SR}), i.e. the "Renieri limit":

$$P_{FEL} = 2e^{-\frac{1}{2}} \frac{\sigma_{\gamma,f}^2 - \sigma_{\gamma,i}^2}{\sigma_{\gamma,f}} P_{SR} \tag{22}$$

where σ_{γ_f} and σ_{γ_i} denote the initial and final energy spread of the beam, respectively. The total emitted synchrotron power is given by [26]:

$$\begin{aligned} P_{SR} &= \frac{1}{3}\frac{e}{\varepsilon_0}\frac{\gamma^4}{\rho} I_a \\ &= 88.46 \cdot 10^3 \ \frac{E^4 I_a}{\rho} \ \frac{[\text{GeV}][\text{A}]}{[\text{m}]} \end{aligned} \tag{23}$$

where I_a is the average beam current and ρ the effective beam radius of the synchrotron. A more sophisticated formula, adapted for an optical klystron reads [27]:

$$
\begin{aligned}
P_{OK} &= \eta_c \frac{f}{\pi(N+N_d)} \frac{\log(G_0/\Gamma)}{G_0/\Gamma} P_{SR} \\
\eta_c &= \frac{\text{mirror transmission losses}}{\text{total transmission losses}} \\
f &= e^{-2\left(2\pi(N+N_d)\frac{\sigma_\gamma}{\gamma}\frac{\lambda}{\lambda_R}\right)^2} \\
\Gamma &= \text{total cavity losses}
\end{aligned}
\tag{24}
$$

Typically the emitted synchrotron radiation is a few kW for a storage ring with a beam-energy up to 1 GeV, e.g. 10 kW for Super ACO operating at 800 MeV. The energy acceptance of a ring, and hence, the maximum possible energy spread, can go up to a few percent. It thus follows that the total emitted FEL power is much lower than the emitted synchrotron power. For example, at Super ACO the total emitted laser power is of the order of 100 mW. Note, however, that this radiation is fully coherent. Hence, the brilliance of this radiation is orders of magnitude higher than synchrotron radiation from an undulator beam-line, see Fig. 3.

It follows from Eqs. (23) and (24) that more power can be obtained at higher beam energy and by allowing a larger increase in energy spread. Note however, that there is a practical limit to both parameters. The energy of the beam can not increase too far without changing the lasing wavelength, see Eq. (1). For this, either the undulator period, or the magnetic field strength, must be increased. The former has the disadvantage that for a given length of the straight section, the number of periods, and hence the gain, is reduced. The latter cause problems with the mirrors, see Sec. 4.2.

An increase of energy-spread requires a significant increase in the energy acceptance of a ring:

$$
\sigma_p \approx \sqrt{\frac{2}{\pi}\frac{e}{mc^2}\frac{V_{rf}}{\alpha h \gamma}} \tag{25}
$$

where h is the harmonic number ($L_c\,\omega_r/2\pi\,c$) and V_{rf} is the total voltage over the rf cavities in the ring. With a too high energy spread, as compared to the energy acceptance of the ring, the lifetime of the beam will be significantly reduced. An increase in energy acceptance is costly since $\sigma_p \propto (P_{rf})^4$.

3.2 The FEL bandwidth

Both the gain bandwidth of the FEL and the eigenmodes of the optical resonator determine the final bandwidth of the FEL where, normally, the gain bandwidth of the laser covers many eigenmodes of the cavity. In this, the SRFEL works similarly to any other type of free-electron laser where the spectrum narrows on successive passes through the undulator. That is, on each pass through the undulator the spectrum of the light pulse is multiplied with the gain spectrum of the laser. In contrast to linac driven FEL's there is no macro-pulse and the process of line-width narrowing can continue over many more round-trips. The line width of an SRFEL is therefore much smaller. Assuming a stable electron beam the line width can narrow down to the transform limit. A study by Dattoli and Renieri [25] predict a laser pulse-width $\sigma_{z,l}$ of

$$
\sigma_{z,l} = \sqrt{\sigma_z N \lambda} \tag{26}
$$

for an undulator with N periods, a wavelength λ, and an electron bunch length σ_z. Note that the laser pulse-duration is much smaller than the electron bunch duration. This is due to the fact that the optical pulse is also multiplied with the longitudinal gain profile of the laser, i.e. the longitudinal electron bunch shape. The corresponding relative bandwidth is

$$\frac{\Delta\lambda}{\lambda} = \frac{1}{\pi}\frac{\lambda}{\sigma_{z,l}} = \frac{1}{\pi}\sqrt{\frac{\lambda}{N\sigma_z}} \quad . \tag{27}$$

In practice the bandwidth is determined by the stability of the beam in the ring, however. Typical relative bandwidths for an SRFEL are in the order of 10^{-4} to 10^{-5} depending on the way the laser is operated. An example is given in the next section. A smaller line width can be obtained by adding additional filters inside the resonator, thus artificially narrowing the gain spectrum. An experiment performed at VEPP3 has demonstrated a relative laser bandwidth of $3{\cdot}10^{-7}$ using an intra-cavity ethalon [28].

3.3 Influencing the FEL output 1: Cavity resynchronisation

From Eq. (23) it follows that the saturated laser power depends on the initial small-signal gain. An optimum gain requires perfect longitudinal and transverse overlap between the optical pulse and the electron bunches. The transverse overlap is mainly determined by the design of the resonator and the machine functions inside the undulator. This will be discussed further in Sections 4 and 5. The longitudinal overlap can only be maintained when the round-trip time of the optical pulses in the laser resonator matches the electron-bunch distance. Hence, the optical cavity length must be matched with the electron bunch distance. Figure 11 depicts this for a storage ring in a two-bunch mode of operation. In that case the resonator length must be one quarter of the circumference of the storage ring. This is, for example, the case for the Super ACO FEL. Other FEL's (e.g. the Duke-FEL and the DELTA FEL) operate in single-bunch mode with a cavity length equal to half the circumference of the ring.

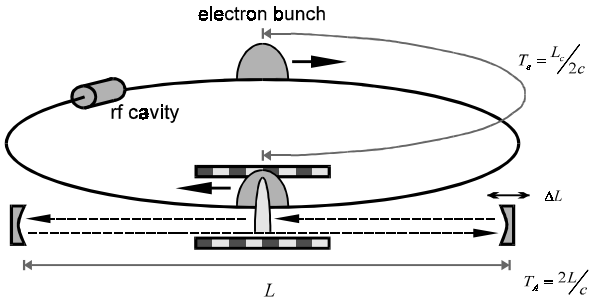

Fig. 11 Longitudinal synchronisation of the FEL: To maintain longitudinal overlap between the optical pulse and the electron bunches, the length of the optical cavity must be tuned to match half the electron-bunch distance. Tuning of the synchronisation can either be done by changing the cavity length or changing the rf frequency of the accelerating field (i.e. changing the distance between successive electron bunches).

As the cavity length is detuned with respect to the spacing between bunches, the longitudinal overlap is reduced and, hence, the small-signal gain is reduced as well. While scanning the synchronisation different (dynamic) behaviour can be observed. An example of the modified output of the Super ACO FEL is given in Fig. 12 [29]. The figure shows the major properties that can be observed in the case of saturation. The main curve displays the average power of the laser. Maximum power is obtained when the cavity length is

synchronised with the bunch distance. When the system is desynchronised, the saturated power level drops. This process is similar to other FEL's. Note that the curve shown in Fig 12 is virtually symmetric around its origin. This is caused by the fact that the electron-bunch length of the Super ACO FEL is long compared to the slippage length. In the case of (much) shorter electron bunches the curve would become more asymmetric, similar to linac driven FEL's.

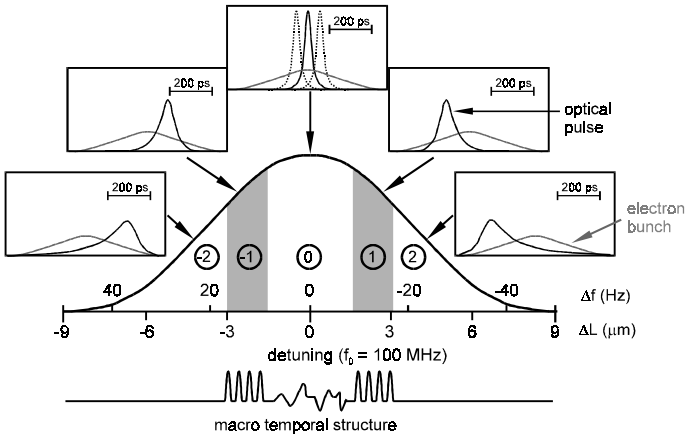

Fig. 12 Longitudinal detuning curve of the Super ACO FEL [29]. The main curve shows the average output power as a function of the detuning. The top graphs give a snapshot of both the electron bunch and the optical pulse at saturation. The bottom curve gives an indication of the macro-temporal structure of the saturated laser output. See text for details.

The graphs above depict the shape of the optical pulse and the electron bunch. The shortest optical pulses are obtained for perfect synchronisation. As the synchronisation changes the optical pulse moves forward or backwards with respect to the electron bunch, depending on the sign of the resynchronisation. Simultaneously the length of the optical pulse increases. This is due to the fact that on one side the optical pulse, on successive round-trips, moves ahead or behind the bunch, will cease to experience gain, and dies out with the ring-down time of the cavity. On the other side of the optical pulse new light is created in the amplification process. Note that the pictures shown are not measured but serve as an example only.

The bottom curve in Fig. 12 shows the macro-temporal structure of the laser. At Super ACO five distinctive zones can be observed. As the laser operates far from synchronisation fairly low power, stable laser output is observed (zones ± 2). As the system is tuned closer to synchronisation a pulsed time-structure is present. In this zone (± 1) a semi-stable competition takes place between the rise time of the optical power, i.e. the increase in energy spread, and its damping given by the damping time of the storage ring. In the next sub-section this process is discussed in more detail. At perfect synchronisation (zone 0) the output power becomes unstable and large irregular fluctuations (~80 %) of the output power are observed. Simultaneously the optical pulse starts to jitter with respect to the electron bunch position. The cause of this jitter is not clear yet but can be counteracted with a feedback system. Note further that the size and number of zones depend on the maximum achievable gain. The zones that are indicated in Fig. 12 are typical for the Super ACO FEL running under optimum conditions. As the available gain drops the central zone becomes smaller or can even

disappear completely. Also at UVSOR, where the gain is lower, the central zone can not be observed [24].

The pulsed time structure that was mentioned in the previous sub-section is an intrinsic effect of the SRFEL and has been explained by Elleaume [31] using a very simple model. This model is based on Eq. (24), which indicates that small changes in the energy spread can have a large effect on the saturated power level. This influence has been modelled as

$$\frac{di}{dt} = \frac{(1-\Sigma)i}{\tau_0}, \qquad \frac{d\Sigma}{dt} = 2\frac{1-\Sigma}{\tau_s}, \qquad \Sigma = \sigma_{\gamma^2} - \sigma_\gamma^2 \tag{28}$$

where i is the dimensionless laser power normalised to unity at saturation. The laser rise time τ_0 is found to be

$$\tau_0 = T/(G_0 - \Gamma) \tag{29}$$

where, additional to the previous definitions, T is the roundtrip time of the optical resonator. τ_0 can be understood as the rise time of the first laser pulse train once the gain has been set higher than the losses. τ_s is the synchrotron damping time. Generally $\tau_0 << \tau_s$ (for example at ACO: $\tau_0 \approx 50$ μs and $\tau_s \approx 200$ ms). Within this restriction the general solution of Eq. (28) is:

$$\Sigma = 1 + \Sigma_0 e^{-t/\tau_s} \cos\left[2\pi \frac{t-t_0}{T_R}\right], \qquad T_R = \pi\sqrt{2\tau_s\tau_0} \tag{30}$$

where Σ_0 is the value of Σ at the beginning of the pulse.

The equations imply that the FEL tends to reach a stable equilibrium state after a series of damped oscillations of period T_R damped with the synchrotron damping time τ_s. An example of a solution of Eq. (30) is given in Fig. 13. It shows that that starting from the laser-off condition the laser intensity has a pulsed behaviour before reaching a stable level. The shape of each pulse is approximated by

$$\frac{i}{i_{\max}} = \cosh^{-2}\left[t\sqrt{\frac{i_{\max}}{\tau_s\tau_0}}\right], \qquad i_{\max} = \frac{(1-\Sigma_0)\tau_s}{2\tau_0} \tag{31}$$

Moreover, it can be shown that the equilibrium state is very unstable and resonant with any perturbation of period close to T_R, so that the laser has in practice a pulsed structure. For example, a noise of 3% affecting the energy spread can account for the randomly pulsed behaviour.

More accurate modelling can be done with the aid of numerical simulation codes, e.g. for the Super ACO case depicted in Fig. 12. A numerical model developed by Hara et al. [32] can make a full prediction of the curves shown in this figure.

3.4 Stabilising the laser: feedback

For use as a light source the central zone is the most interesting since it provides the highest power levels as well as the narrowest line width. The main drawback is the instability of the laser power and the temporal jitter. For this reason Billardon et al. [30] have developed a feedback system capable of stabilising temporal jitter. In the feedback system, a dissector measures the position of the optical pulse, relative to the positron bunch. When the optical pulse moves, the position of the bunch is adjusted accordingly through a change in the rf frequency. With the feedback the laser becomes much more stable. Power level fluctuations,

for example, drop below 5 %. Figures 14 and 15 show the change in temporal jitter, measured with a streak-camera and a dissector, respectively. In Appendix A, the diagnostic equipment is described. Table 3 gives a summary of the output parameters of the laser. Note the reduction in optical pulse length with the feedback in zone 0.

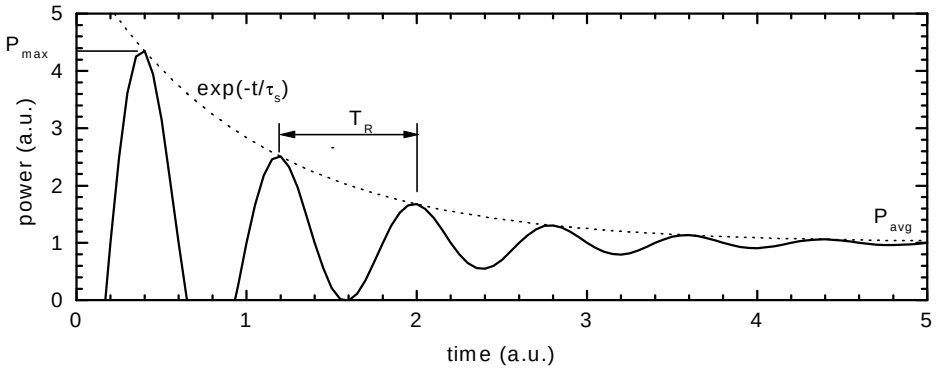

Fig. 13 Evolution of the optical power of the laser: the rise time of the laser and the damping of the synchrotron lead to a damped oscillation of the laser power as predicted by Eqs. (28) to (31).

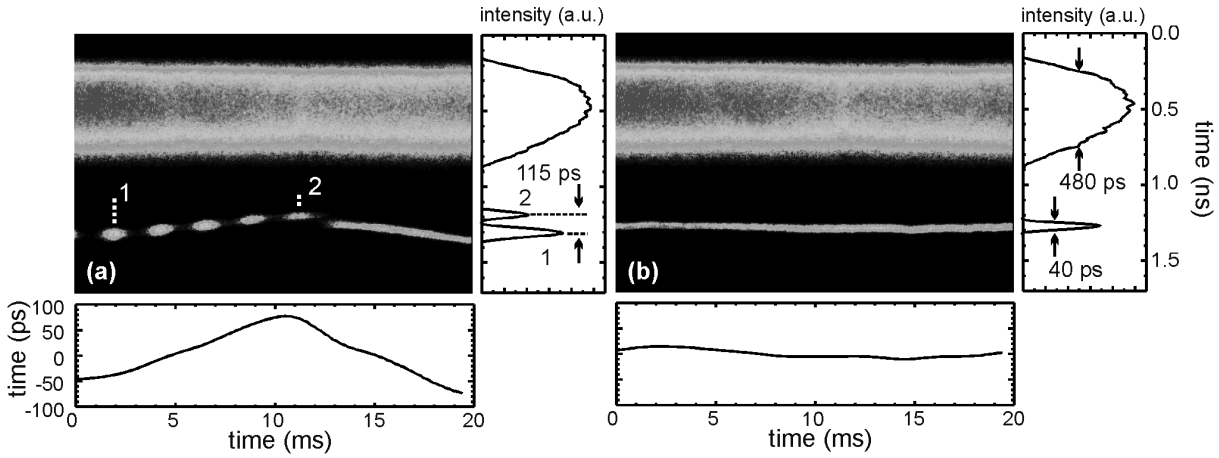

Fig. 14 Results of the longitudinal feedback system installed at Super ACO measured with a double sweep streak-camera: (a) without feedback and (b) with feedback. The fast sweep is along the vertical axis and the slow sweep along the horizontal axis. The photo's show both the positron bunch (top) and the laser pulse (bottom). Note the difference in duration between the positron bunch and the laser pulse.

Table 3

Temporal and spectral features (bandwidth and drift) of the Super ACO FEL operated at 350 nm [33]

Zone	σ_t (ps)	σ_λ/λ ($\times 10^{-4}$)	Δ_λ/λ ($\times 10^{-4}$)	**Macro structure**	**Remarks**
0	17			Cw	Feedback
0	20	0.3-1.2	< 3	Cw	No feedback: Jitter up to 200 ps
1, -1	25-35	0.6-1.5	6-9	Pulsed	Rapid wavelength shifts
2, -2	35-45	0.9-1.5	< 3	Cw	Low power

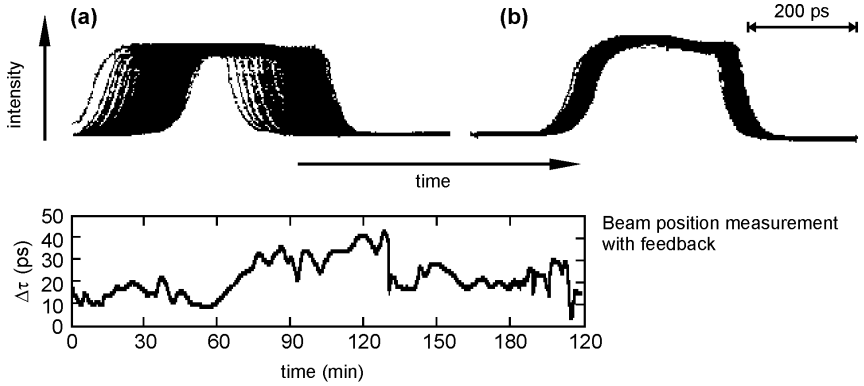

Fig. 15 Results of the longitudinal feedback system installed at Super ACO [30]. The top graph shows the jitter of the base of the optical pulse measured with a dissector (in the centre of the pulse the detector is saturated) without feedback (a) and with feedback (b). The bottom graph shows the jitter of the optical pulse over two hours with feedback. Without feedback the jitter exceeds the positron bunch duration of 200 ps.

3.5 Influencing the FEL output 2: Q-switching (gain-switching)

One interesting consequence of the laser instability is the possibility of driving these oscillations externally, i.e. Q- or gain-switching. By modulating the optical gain with a period of the order of magnitude of T_R it is possible to obtain very regularly spaced and reproducible pulses, see Fig. 16. The Q-switching of SRFEL's has two great advantages over working with the natural time structure: (i) the laser is stabilised and (ii) the laser peak power is enhanced by several orders of magnitude. If T_0 is the Q-switching period a maximum is reached at $T_0 \sim \tau_0$ and the peak power enhancement is about $\tau_s/4\tau_0$. This factor is ~10^3 for the ACO experiment (and will be about the same on future experiments) although only 10^2 could be reached in practice. Remember that the higher the small signal gain g_0, the smaller the rise time τ_0 and the bigger the peak power enhancement. However, the estimates given above do not take into account saturation by over bunching in the case of a high-power SRFEL. When the dimensionless laser field $|a|$ [35] ($|a| = 4KN_u eKL_u|E|/\gamma^2 mc^2 \approx 0.1$ on ACO, Q-switched regime, where $|E|$ is the optical field strength) becomes of the order of unity, over-bunching will occur which will modify the above results. In most cases, use of the Q-switching technique will drive the peak power up to the over-bunching limit.

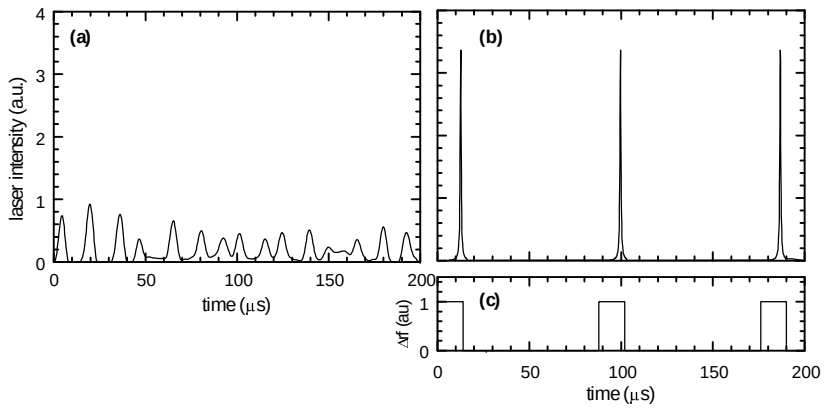

Fig. 16 Time record of the ACO laser intensity [34] for (a) "natural" operation and (b) low-frequency gain switched operation. The trace in (c) shows the switching of the gain through a

change of the longitudinal overlap between the optical pulses and the bunches, i.e. changes of the rf frequency.

4. THE RESONATOR

The most commonly used resonator in an FEL is the stable two-mirror normal-incidence resonator, see Fig. 17, which will be discussed in more detail in Sec. 4.1. Its main advantages are its straightforward design and the possibility to obtain low loss (less than 1%) resonators with the aid of multi-coated dielectric mirrors. Furthermore, two-mirror normal-incidence resonators are also common practice in other laser systems. There are also some drawbacks to the design, however. For example, in Sec. 4.1 it will be shown that the tolerances to resonator dimensions become more critical as the resonator length increases relative to the undulator length. This is specifically an important factor in the SRFEL since more space is required to include elements for the electron beam optics (e.g., quadrupoles and dipoles). Furthermore, the cavity length must be adjusted to match half of the bunch spacing in the storage ring in order to obtain overlap between the optical pulses and the electron bunches on each passage through the cavity. Other, and more fundamental, drawbacks are related to the optics required for the resonator. In Sec. 4.2 the two most prominent problems are discussed, i.e. the occurrence of mirror degradation due to the harmonics present in the spontaneous undulator radiation and the lack of available high-reflecting optics at shorter wavelengths. Because of these problems, other (resonator) schemes have been considered of which a brief overview is given in Sec. 4.3.

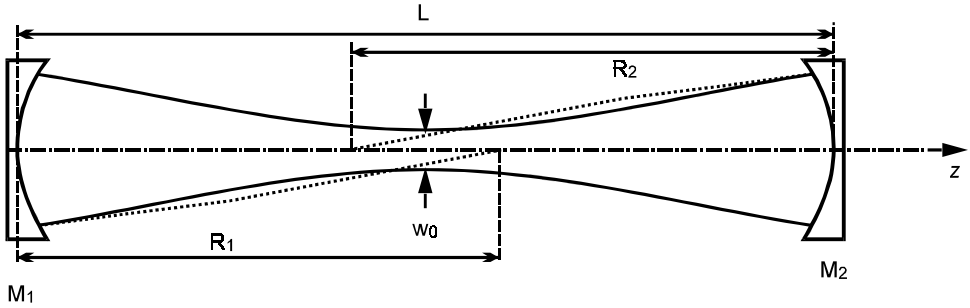

Fig. 17 Schematic diagram of a cavity defined by the mirrors M_1, M_2 and the cavity length L. The mirrors have a radius of curvature R_1 and R_2, respectively.

4.1 Standard resonator geometry

In the two-mirror normal-incidence resonator two curved mirrors are used to obtain a stable periodic focusing system, see Fig. 17. If the transverse dimensions of these mirrors are large enough and edge diffraction effects can be neglected it can trap the lowest or higher order Gaussian modes which bounce back and forth between the two mirrors. An overview of the properties of such systems can be found in the Refs. [36, 37, 17]. Here the most important aspects for the FEL are summarised.

The resonator of Fig 17, can be characterised by its length L and the radius of curvature of both mirrors R_1 and R_2. As discussed in Sec. 2.1 it is important to minimise the average transverse optical mode area to optimise the small-signal gain of the FEL. For this the so-called Raleigh length β_0 plays an important role, i.e. the distance over which the transverse mode-area of a TEM_{00} mode increases with a factor 2 relative to the minimum mode area in the waist.

$$\beta_o = \sqrt{\frac{L(R_1 - L)(R_2 - L)(R_1 + R_2 - L)}{(R_1 + R_2 - 2L)^2}} \tag{32}$$

Note that β_o plays the same role as the machine functions $\beta_{x,y}$ used to describe the electron beam optics of the ring. The minimum spot size (waist) of the E-field of a TEM_{00} mode can be found to be:

$$\sigma_0 = \sqrt{\frac{\lambda\beta_o}{2\pi}} \tag{33}$$

with the waist position, relative to the centre of the cavity, given by

$$z_0 = \frac{1}{2}\frac{R_1 - R_2}{R_1 + R_2 - 2L}L\,. \tag{34}$$

Note that for a symmetric cavity ($R_1 = R_2$) the waist position is in the centre of the cavity ($z_0 = 0$). The transverse mode area at an arbitrary position is

$$\Sigma_A(z) = \pi\sigma_0^2\left[1 + \left(\frac{z - z_0}{\beta_0}\right)^2\right] \tag{35}$$

To optimise the gain one has to optimise the filling factor, i.e. maximise $\langle \Sigma_e / \Sigma_A \rangle_{L_u}$ where the brackets denote the average over the whole undulator. It can be deduced that the optimum Raleigh length can be approximated by $\beta_0 \approx L_u/3$ [17] leading to the result presented in Sec. 2.2.

Next it is also important that the resonator is stable, i.e. that it can store the optical field on multiple passages through the resonator. It is customary to describe the stability of a two-mirror resonator with the so-called stability parameter g [37]:

$$g_1 = \left(1 - \frac{L}{R_1}\right), \qquad g_2 = \left(1 - \frac{L}{R_2}\right) \tag{36}$$

where, for a stable resonator, the following condition needs to be fulfilled:

$$0 \le g_1 g_2 < 1. \tag{37}$$

In an FEL the cavity length is generally much longer than the undulator length since space is required to install additional components for the electron beam such as quadrupolar lenses and dipoles. This is specifically true for SRFEL's since the cavity length must also equal half of the spacing between successive electron bunches. The difference between the undulator length and the cavity length can, therefore, be considerable. For example at Super ACO the undulator has a total length of 3 m with a resonator length equal to 18 m. For the Duke FEL project an undulator of 15 m with a cavity length of 50 m is anticipated.

The requirement of $\beta_0 \approx L_u/3$ and $L >> L_u$ generally leads to a situation where $g_1 g_2 \to 1$ and, hence, a nearly unstable cavity. The effect of this is illustrated in Fig. 18. As the resonator length increases with respect to the undulator length it becomes more difficult to obtain the optimum filling factor, firstly because the tolerances on the radius of curvature become more restricted (Fig. 18b) and secondly because the resonator comes closer to the stability limit (Fig. 18c).

When a cavity approaches the stability limit, it also becomes more sensitive to misalignment errors. The effect of misalignment is illustrated in Fig. 19. The optical axis in a two-mirror resonator is, by definition, the line passing through the centres of curvature C_1 and C_2 of the two end mirrors. The quadratic base curvatures of the two mirrors are centred on or are normal to this axis. If the cavity also contains any kind of aperture (including the apertures defined by the mirrors themselves), rotation of an end mirror will translate the optical axis relative to this aperture or, alternatively, will cause the aperture to be effectively off centre with respect to the resonator axis. The presence of an off-centre aperture will tend to produce resonator eigenmodes that are mixtures of the even and odd eigenmodes of the aligned resonator. From simple geometry considerations it can be deduced how far the optical axis will be translated and rotated by a small angular rotation of either end mirror. Let θ_1 and θ_2 be the small angular rotations of the two end mirrors and Δx_1 and Δx_2 be the small sideways translations of the optical axis at the point where it intercepts the end mirrors, as shown in Fig. 19. Alternatively, Δx_1 and Δx_2 can represent the off-centre translations of the apertures at those two mirrors. From Fig. 19 and some simple geometry we can then evaluate these displacements as [36]:

$$\Delta x_1 = \frac{g_2}{1-g_1 g_2} L\,\theta_1 + \frac{1}{1-g_1 g_2} L\,\theta_2$$
$$\Delta x_2 = \frac{1}{1-g_1 g_2} L\,\theta_1 + \frac{g_1}{1-g_1 g_2} L\,\theta_2 \qquad (38)$$

One criterion for judging the seriousness of misalignment effects is to compare the transverse displacement of the centre of the cavity with the optical waist size and the transverse electron beam dimensions.

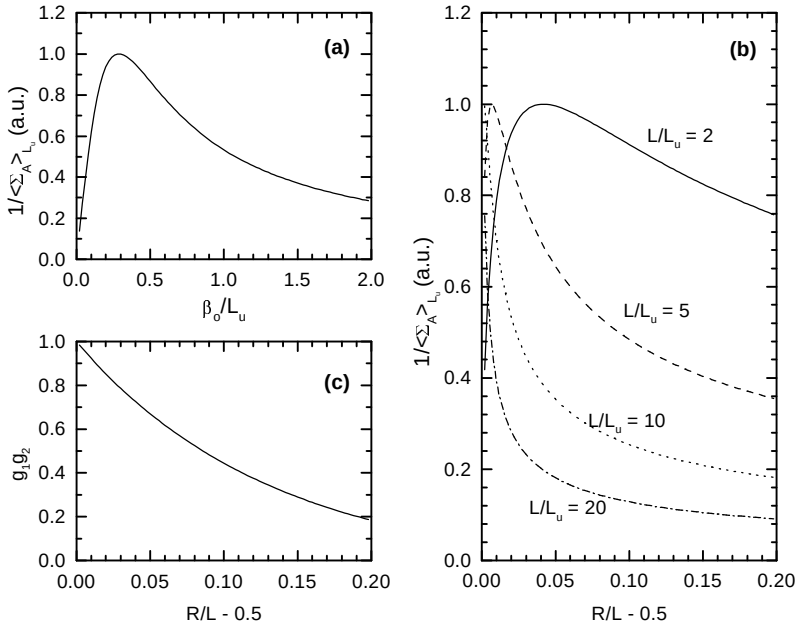

Fig. 18 Influence of the resonator geometry on the FEL gain and the resonator stability: (a) The filling factor as a function of the Raleigh length, see Eq. (32) normalised with respect to the undulator length L_u. (b) Filling factor as a function of the radius of curvature of the mirrors

for a symmetric cavity, i.e. $R = R_1 = R_2$, for different undulator lengths with respect to the cavity length L. (c) The resonator stability parameter a function of the radius of curvature. Note that $(R/L - 0.5) = 2(\beta_0/L)^2$.

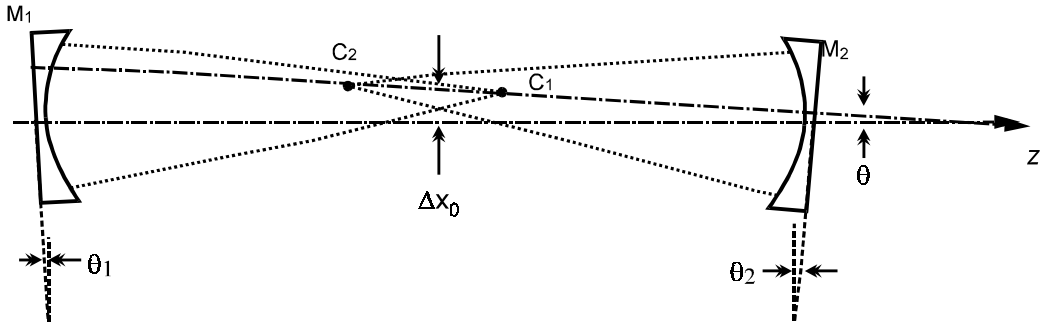

Fig. 19 Geometry of a misaligned optical cavity

The angular displacement of the resonator axis that can be important in evaluating far-field pointing accuracy, for example, can be evaluated from [36]:

$$\theta = \frac{\Delta x_2 - \Delta x_1}{L} = \frac{(1-g_1)\theta_1 - (1-g_2)\theta_2}{1-g_1 g_2}. \tag{39}$$

This parameter can be specifically important for user light sources where the FEL radiation has to be transported over large distances to a user experiment. Note that the sensitivity of these angular misalignment blows up as $g_1 g_2 \rightarrow 1$, i.e. as the resonator design approaches the stability boundary. Note further that with $g_1 g_2 \rightarrow 1$ and $\sigma_0 <<$, see Eq. (33), it is conceivable that the resonator will be more sensitive to higher-order transverse mode which impedes both the laser gain and/or the stability at saturation. At Super ACO such modes are common. The order of the mode and its stability depends on the beam current: small changes at the mirror due to temperature induce mechanical stress, see Sec. 4.2.

Finally it is important to consider the mirror dimensions since too small mirrors will cause radiation leakage along the edges of the mirrors. These losses can be evaluated with the aid of the resonator Fresnell number N_f:

$$\frac{\text{resonator mirror surface area}}{\text{confocal TEM}_{00}\text{ mode area}} = \pi N_f \tag{40}$$

To reduce cavity losses a large Fresnell number, i.e. $N_f > 10$ is preferable, see Fig. 20.

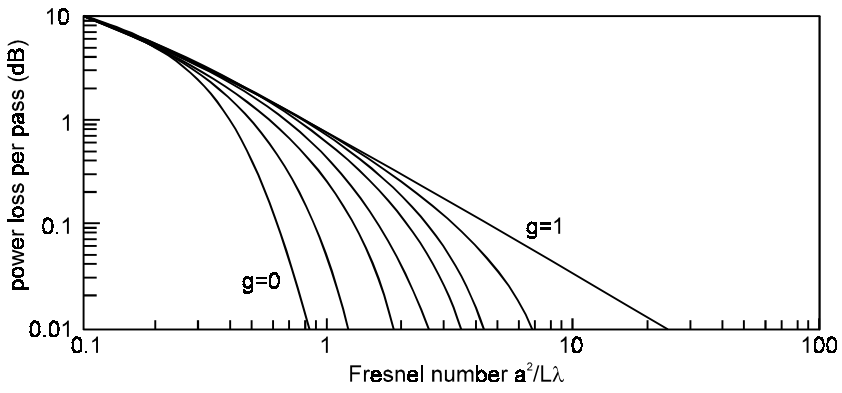

Fig. 20 Power loss per round trip (measured in dB) versus Fresnell number for a TEM_{00} mode in a two-mirror symmetric resonator, i.e. $R_1 = R_2$, with g-values ranging from g = 0 (confocal resonator) to g = 1 (planar resonator). The intermediate g values are g = 0.5, 0.8, 0.9, 0.95, 0.97 and 0.99 respectively [36].

4.2 Optics

SRFEL's are low gain devices, i.e. a laser where a resonator is required to reach saturation on multiple passes. The problem of making good mirrors for the visible to the VUV spectral region is a difficult one and deserves at least a separate chapter. For general information the reader is referred to textbooks and review articles [3840]. Specially for the UV and VUV spectral region it becomes more difficult to find suitable materials for mirrors. As a result the operational wavelength range of the SRFEL is reduced. An overview of the state of the art mirror technology is given in Fig. 21.

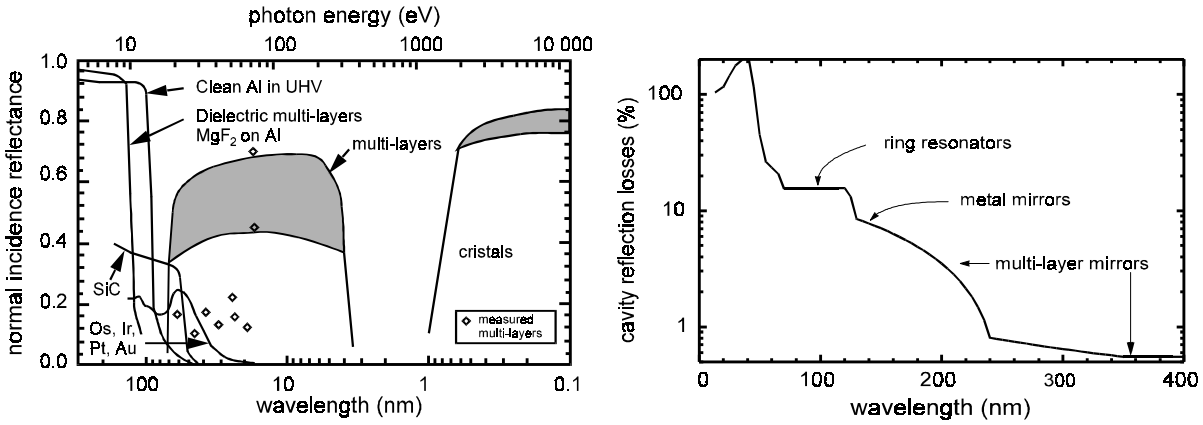

Fig. 21 Reflectivity of normal-incidence optics [40] and the estimated cavity loss due to absorption at the mirror surface. For details on ring-resonators, see Sec. 4.3.

Apart from these problems there are additional ones which arise due to the nature of the SRFEL:

- The gain of a SRFEL is, at present, up to a few percent. To obtain the lasing threshold condition, i.e. cavity losses < gain, highly-reflecting mirrors are required, i.e. multi-coated mirrors. Highly-reflecting multi-coated mirrors have a narrow spectral bandwidth and, as a consequence, impede the wavelength tunability of the FEL.
- As will be explained below, mirrors of an SRFEL are exposed to a harsh environment of high power radiation ranging from the visible to the X-ray region. As a result thermal effects and mirror damage or mirror degradation forms a serious problem in the operation of the SRFEL.

To overcome the first restriction metal mirrors, e.g. coated Al mirrors [40], could be used. However, the losses associated with these types of mirrors are of the order of a few percent and all SRFEL's that are presently operational do not have sufficient gain to use such mirrors.

A multi-coated mirror consists of a stack of Fabry-Perot interferometers where each layer has an optical thickness of $\lambda/4$. Two different layers are deposited alternately, one with a low- and one with a high index of refraction. The residual diffusion and absorption in the layers limit the maximum reflectivity. For a mathematical treatment of such mirrors refer to

Ref. [41]. In the visible region reflectivity's as high as 99.95 % can be obtained. However, in this case the ratio of the transmission over the losses is very low and does not permit good energy extraction [42]. Multi-layers with a reflectivity over 99.5 % are currently manufactured down to a wavelength of 240 nm. An overview of some materials suitable for mirrors in the UV is given in Table 4.

Table 4

Optical constants of oxide layers deposited by reactive sputtering [43]

	SiO_2		Al_2O_3		$[Hf_xSi_{1-x}]O_2$		HfO_2		ZrO_2		Ta_2O_5		TiO_2	
λ (nm)	n	k $\times10^{-4}$	n	k $\times10^{-4}$	n	k $\times10^{-4}$	n	k $\times10^{-4}$	N	k' $\times10^{-4}$	n	k $\times10^{-4}$	n	k $\times10^{-4}$
200	1.50	0.00	1.83	29.1	2.13	78.0	2.51	152	—	—	—	—	—	—
300	1.47	0.00	1.70	11.9	1.99	9.8	2.12	33.7	2.32	37.0	2.38	45.6	—	—
400	1.46	0.00	1.65	3.7	1.90	4.4	2.05	12.3	2.21	23.6	2.26	5.3	2.7	21.6

Apart from a good choice of non-absorbing materials suited for use as layers for the multi-coatings, the intrinsic losses of the mirrors are also determined by the surface roughness of the mirror, which determines the diffusion at the mirror surface. Especially at shorter wavelengths this aspect becomes more important [45]. An example of a multi-coated mirror with a central wavelength of λ = 300 nm is given in Fig. 22. From the plot it follows that the mirrors have an intrinsic loss of 0.4%. However, as the surface roughness goes up the losses increase. Above a rms average roughness of 0.2 nm the scattering losses dominate the absorption losses of the mirror.

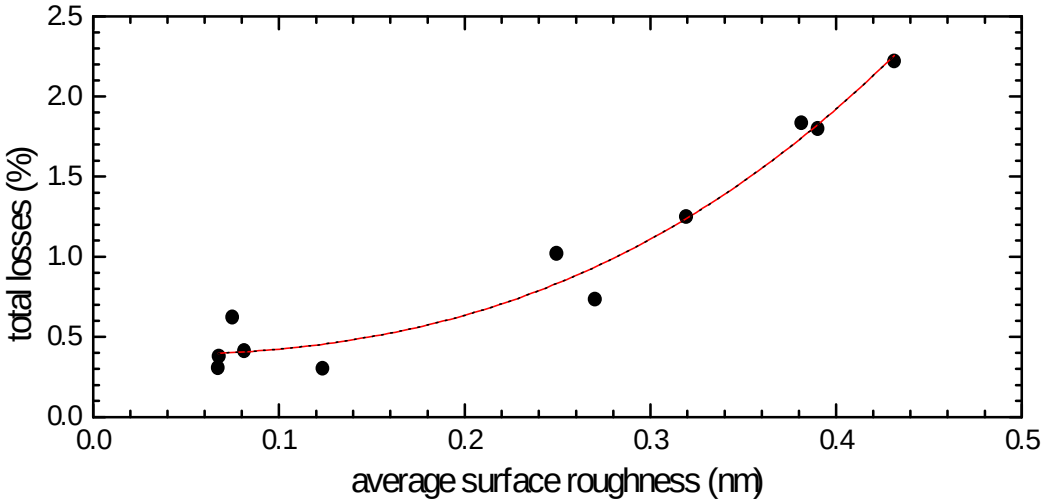

Fig. 22 Total losses as a function of the average rms surface roughness of a mirror at λ = 300 nm. The example given involves a multi-layer mirror with HfO_2/SiO_2 layers [44].

In an SRFEL it is not sufficient to produce mirrors which have an initially high reflectivity coefficient. While operating the laser the resonator mirrors can be exposed to a very intense flux of spontaneous radiation emitted by the undulator. For this it is important to remember that the typical beam energy of a storage ring will be of the order of (at least) a few hundred MeV. Hence, the total emitted power from an undulator is given by [26]:

$$P_u\,(\mathrm{W}) = 7.28\,E^2\,(\mathrm{GeV})\,NI\,(\mathrm{A})\,\frac{K^2}{\lambda_u\,(\mathrm{cm})} \tag{41}$$

where the same notation as in Sec. 2 has been used.

From Eq. (41) it follows that the spontaneous radiation can easily go up to a level of several (tens of) Watts. All this radiation will be deposited on the resonator mirror at the down-stream side of the undulator and thermal effects can occur. Note that due to the low gain of the SRFEL it is not possible to install the resonator mirrors outside the vacuum system. Hence, mirrors can only be cooled by either the mirror support or by thermal radiation. Since the radiation stored in the cavity is extracted through transmission of the mirrors it is important that both the mirror support and the mirror substrate have a good thermal conductivity. At Super ACO, for example, 18 W of spontaneous radiation hits the downstream mirror. As a result isolated mirrors on a SiO_2 substrate were heated with ΔT = 80ºC relative to room temperature. Under the same conditions mirrors on an Al_2O_3 substrate were heated by ΔT = 35 ºC. With a mirror support with a good thermal contact the rise in temperature could be reduced to ΔT = 58 ºC and ΔT = 5 ºC, respectively [46].

Next, the spectrum of the radiation plays an important role as well. The spontaneous radiation of a planar undulator does not only contain the fundamental harmonic such as given in Eq. (1) but also a large number of harmonics. For on-axis radiation (θ = 0) the harmonics per opening angle Ω are given by [26]:

$$\left.\frac{d^2I}{d\omega d\Omega}\right|_{\theta=0} = \frac{1}{4\pi\varepsilon_0}\frac{4(e\gamma N)^2}{c}\sum_{n=1,3,\ldots}^{\infty} F_n(K)\left(\frac{\sin\nu_n}{\nu_n}\right)^2$$
$$F_n(K) = 4\xi_n\left(J_{\frac{n+1}{2}}(\xi_n) - J_{\frac{n-1}{2}}(\xi_n)\right) \tag{42}$$

where n denotes the harmonic number. The parameters ξ_n and ν_n are given by:

$$\xi_n = \frac{1}{2}\frac{nK^2}{1+K^2}$$
$$\nu_n = n\pi N\frac{\lambda_n - \lambda}{\lambda_n} \tag{43}$$

A graph of Eq. (42) is presented in Fig. 23. Especially for SRFEL's the undulator strength K can be high because of the high energy of the beam stored. As a consequence the power of the harmonics radiated by the undulator can be high as well. For this it is convenient to recall the critical wavelength λ_c or critical harmonic n_c, i.e. the wavelength for which half of the power is radiated at wavelengths shorted than this value.

$$\lambda_c\,(\mathrm{nm}) = \frac{1.86}{B_u\,(\mathrm{T})\,E^2\,(\mathrm{GeV})}$$
$$n_c = \frac{3}{2\sqrt{2}}K(1+K^2) \tag{44}$$

In Table 5 it can be seen that for typical SRFEL experiments the critical wavelength is much shorter than the fundamental wavelength. Generally the mirror absorbs these harmonics and mirror damage can occur.

An example of such mirror degradation is shown in Fig. 24. At present mirror degradation can not be avoided. However, it is possible to produce multi-coated mirrors that are more resistant. This topic is still very much under development. One of the aspects that play an important role is the fabrication process involved. Mirrors fabricated with an ion-beam sputtering method are more resistant to synchrotron radiation, see Fig. 25. The vacuum level, i.e. the number of residual gas molecules near the mirror surfaces also influences mirror degradation. Ultra-high vacuum is required in order to reduce the absorption of residual molecules such as carbon which reduces the overall reflectivity of the mirrors. However, loss of reflectivity due to carbon contamination can be recovered by exposing the mirror surface to RF-discharged oxygen plasma [46-48].

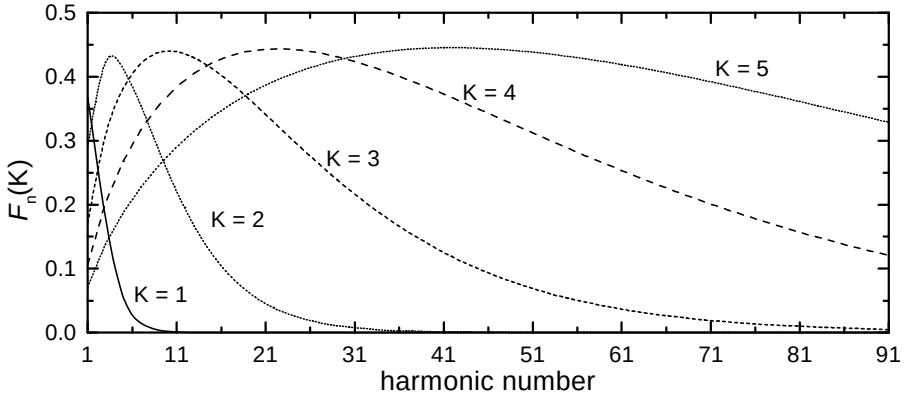

Fig. 23 Contents of the on-axis harmonics of a planar undulator for several values of the undulator strength, see Eq. (42)

Table 5

Undulator radiation for various SRFEL experiments. Estimated values are given in italic [46]

Experiment	**Beam char.**		**Undulator characteristics**			**Radiation characteristics**			
	E (MeV)	I (mA)	λ_u (cm)	N	K	P_u (W)	λ_c (nm)	λ_{FEL} (nm)	P_{FEL} (mW)
Super ACO	800	100	12.9	20	5.0	18	7.1	350	100
UVSOR	500	20	11.1	16	2.9	0.4	26.6	300	0.2
VEPP3	350	40	10.0	67	1.6	0.6	89.3	250	2.5
DELTA	*700*	*100*	*25.0*	*17*	*2.1*	*1*	*54.2*	*213*	—
Duke	*1000*	*100*	*10.0*	*67*	*6.6*	*210*	*2.6*	*300*	—

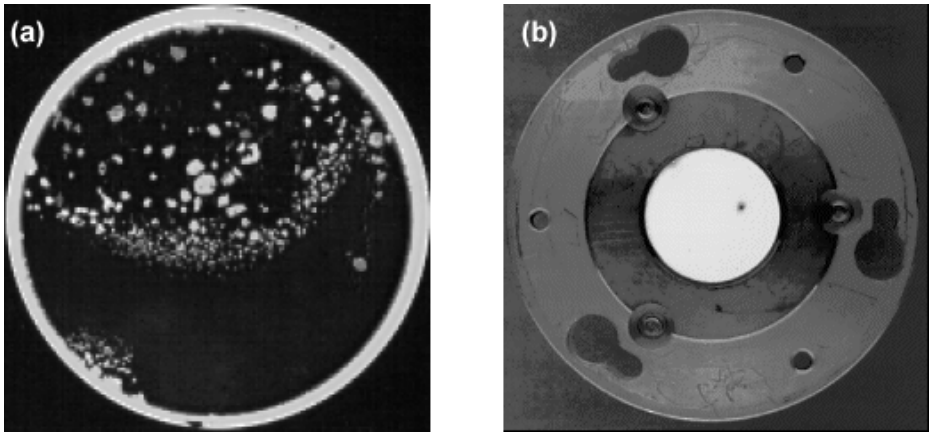

Fig. 24 Examples of mirror degradation due to the spontaneous undulator radiation. (a) Severe degradation of a test mirror deposited on a SiO_2 substrate. (b) Photo of a mirror in its support after 60 hours of FEL operation showing the presence of a large carbon spot [26].

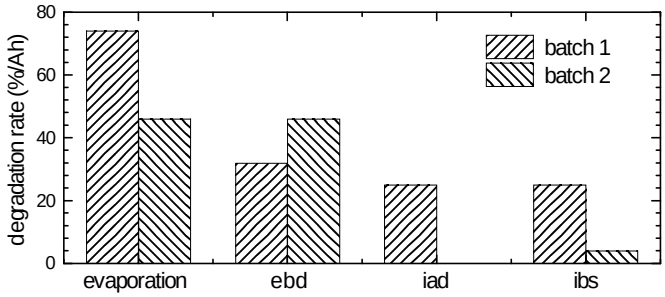

Fig. 25 Summary of the degradation rates applying to different deposition techniques: classical evaporation, electron beam deposition (ebd), ion-assisted deposition (iad) and ion beam sputtering (ibs) [46].

4.3 Alternative solutions

The problems related to the optics remain a difficult one. Nevertheless several solutions have been considered and/or implemented in FEL experiments. Some of these ideas are listed below.

Helical undulators

Helical undulators have the advantage of having a higher gain since the periodic dephasing of the electrons with respect to the optical wave is not present. Next, the use of a helical undulator or optical klystron can significantly reduce the amount of harmonics emitted. The main disadvantages of the helical undulator or optical klystron are a more complex design and a reduced flexibility to change the undulator strength *K*. At present only the UVSOR SRFEL experiment employs such a device as an OK [49] and lasing has been obtained down to a wavelength of 239 nm. A calculation on the expected transverse spectral distribution of this device is shown in Fig. 26. Note the different distribution of the high-energy photons in the form of a ring. It is thus possible to filter out this radiation with the aid of an iris, thus reducing the mirror degradation on the mirror surface due to the interaction of these photons with residual gas molecules near the mirror surface.

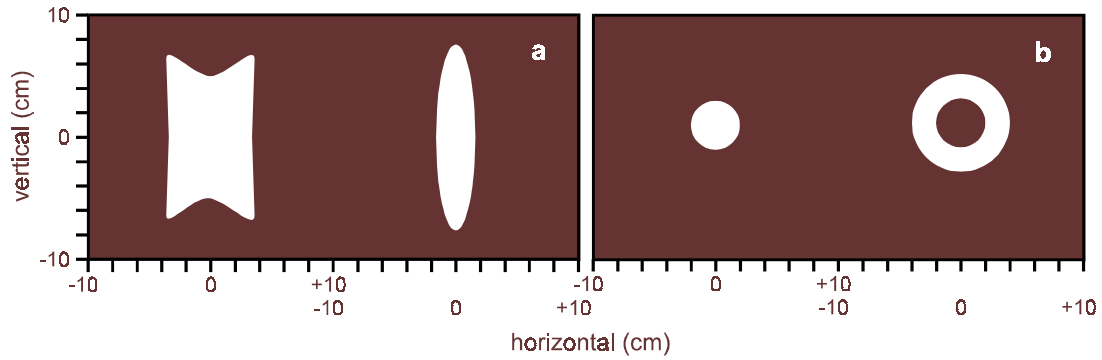

Fig. 26 Calculated spatial distribution of radiation from a planar OK (a) and a helical OK (b) such as in use at the UVSOR SRFEL experiment [49]. The left-hand sides of both figures show the integrated intensity of the low energy photons (< 10 eV). The right-hand side depicts the high-energy photons (10-200 eV).

Alternative resonator design

An alternative resonator design can also enhance the performance of the SRFEL. Two options are depicted in Figs. 27 and Fig. 28. In Fig. 27 two corner-cube resonators replace the normal-incidence end mirrors of the resonator. This design has been proposed for the CEBAF linac driven FEL [50]. The main advantage of this design is the increased stability. In the case where the cavity is filled with multiple optical pulses it also has the advantage that the return path of the light is separated from the electron beam. Hence, Compton back scattering with electrons passing through the undulator while the optical pulse returns can not take place. Obvious disadvantage is the increased resonator losses since the number of reflections are increased from two to six. At present no FEL system in the visible or UV was capable of using such a design due to lack of gain.

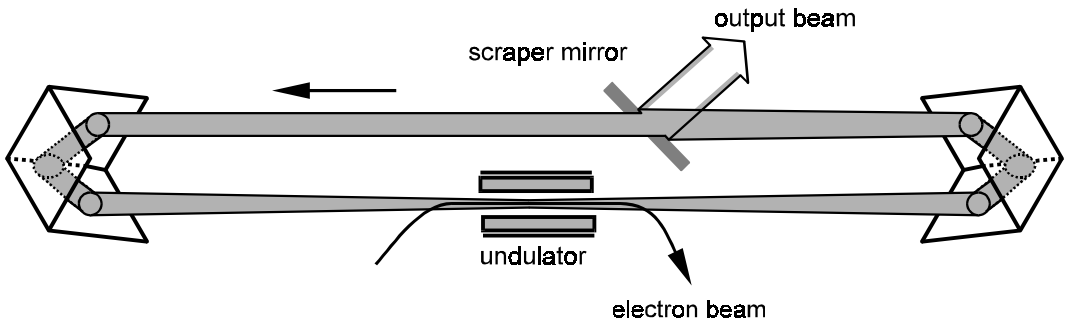

Fig. 27 Self-imaging confocal unstable ring FEL resonator with corner-cube reflectors [50]

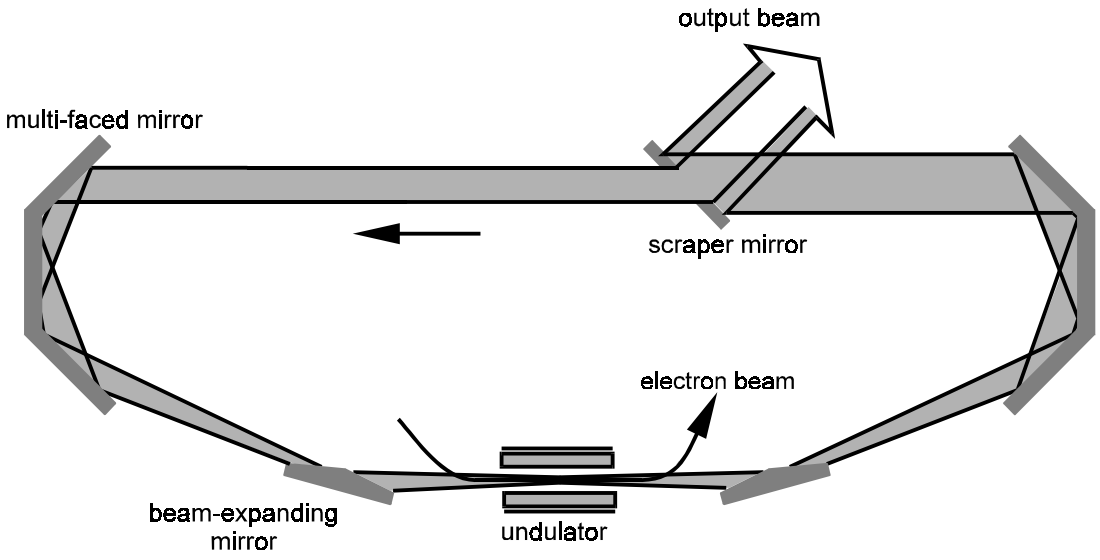

Fig. 28 Grazing incidence or ring resonator [51]

The most commonly considered alternative is the so-called whispering-mode or ring resonator, Fig. 28. In laser technology ring resonators were understood and demonstrated very early on, and have since been extensively developed for applications in ring-laser gyroscopes [36]. For free-electron lasers this type of resonator is not much used, however. Until now only one FEL experiment has made use of such a resonator at a wavelength of 640 nm [51]. Nevertheless, ring resonators have several advantages [36, 52]:

- Increased cavity design flexibility, alignment insensitivity, and insensitivity for higher order transverse modes.
- Higher level of power extraction.
- Possible operations with grazing incidence reflectance at wavelengths where no optical material for normal-incidence mirrors are available.
- Separation of the return path of the light-pulse. This can be specifically advantageous for cavities with a multiple of optical pulses where Compton back-scattering of the light pulses with the electron beam needs to be avoided.

The main disadvantage is the complexity of the design, especially the initial alignment that is required to stack the optical pulse in the resonator.

Harmonics generation

In Fig. 23 it was seen that the (planar) undulator of the FEL is an excellent harmonics generator. Furthermore, as the electrons pass through the undulator they are bunched on the scale of the fundamental wavelength. This also causes an increase in the component of higher order modes in the longitudinal density distribution of the electron beam. As explained above the optics cause a serious problem for lasing at shorter wavelengths. As an alternative it is, therefore, worthwhile considering the options for extracting harmonics out of the FEL, either through seeding with another laser or by FEL operation at a longer fundamental wavelength.

One of the options would be to use an external laser to produce a substantial up-conversion in the FEL interaction region. In the first demonstration [53, 54] of the technique, a YAG laser bunched the electrons either on the infrared or the green line, and emission was observed on the harmonics of the bunching frequency. Although the efficiency was low (10^5 to10^7 photons per pulse were obtained), better results are expected in future experiments.

As an alternative to the seed laser it would be better to employ the FEL itself. If the FEL intensity builds up to saturation, the laser generates its own harmonics. Reasonable conversion

efficiencies have now been reported from the infrared FEL oscillator experiments. This approach has the advantage of tunability since an external laser is not required. It will also be possible to reach the highest frequencies this way since the FEL itself is anticipated to be the shortest-wavelength laser available. No such coherent harmonic radiation was observed at ACO since the laser saturated due to bunch lengthening long before saturation due to over-bunching could be reached. However, if sufficient gain is available, SRFEL's can reach high peak power in the Q-switched mode and will therefore produce strong harmonic emission. Possible solutions for extracting the harmonics are sketched in Fig. 29 where in (a) an intra-cavity ethalon is used to extract the harmonics out of the cavity. Note that this option only works if there is sufficient gain as the ethalon induces extra cavity losses. For example at Super ACO lasing in this mode of operation has not yet been demonstrated due to too high cavity losses as compared with the maximum obtainable small-signal gain. In Fig. 29 an additional undulator with a 3- or 5-times shorter period has been drawn. In this situation the harmonic compound of the electron beam, generated in the FEL interaction, is amplified in the second undulator. Note that for this option careful tuning of the saturated power level of the fundamental wavelength is required in order to avoid over-bunching before the electrons enter the second undulator: $|a| = 4KN_u eKL_u|E|/\gamma^2 mc^2 < 1$ [35].

5. DESIGN OF THE STORAGE RING

From Eq. (10) and Eq. (17) it follows that the gain of an FEL scales with N^2 in the case of an undulator, and with N in the case of on optical klystron. Hence, a high gain can only be obtained in long straight sections where sufficient space is available for the undulator. To avoid energy dependent behaviour (the FEL extracts energy from the beam and increases the energy spread) it is also convenient if this section is dispersion free. From Sec. 2 it follows that an optimum gain can only be obtained with a high peak current in combination with a low energy spread and emittance, i.e. with an as high as possible density in phase space. For a detailed discussion on the optimisation of a storage ring with respect to such parameters the reader is referred to the other chapters of these proceedings. Here the parameters specifically important for the FEL are discussed. In Sec. 5.1 and 5.2 an overview of some aspects to obtain a high peak current and a low energy spread and emittance is given. The optimum performance of the SRFEL also requires a maximum transverse overlap between the optical pulse and the electron beam. This optimisation process is presented in Sec. 5.3.

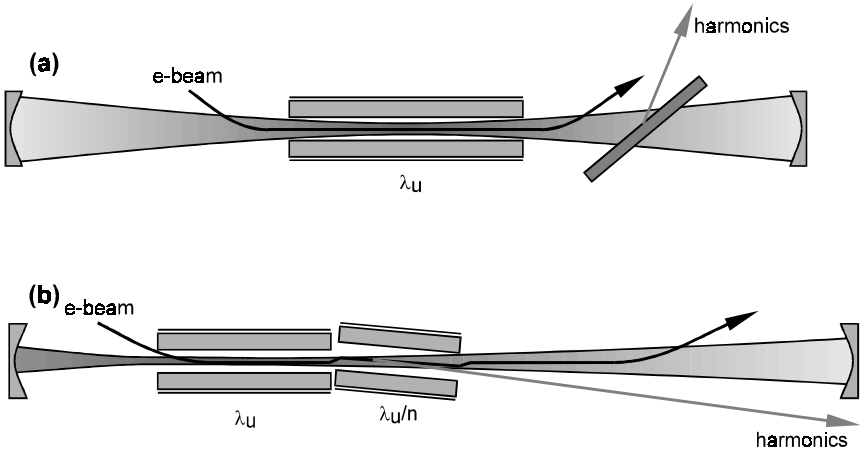

Fig. 29 Possible options for harmonics generation using the a free-electron laser that lases on the fundamental wavelength as a seed: (a) reflecting the present harmonics through an intra-cavity ethalon, (b) enhancing the output of an undulator tuned to a wavelength of λ/n by using

the electron beam that has passed through the laser as a seed. Note that the undulator has been set at a small angle so that the harmonics are not intercepted by the resonator mirrors.

5.1 Ring geometry

One of the easiest ways to increase the peak current, while keeping the average current low, is to reduce the number of bunches in the ring. Maximum current can be obtained in a singe-bunch mode of operation. For this it is important to keep in mind that the resonator length must match half the distance between successive bunches. For large storage rings this implies very long cavities. Assuming a standard two-mirror resonator, see Sec. 4.1, it is difficult to keep such a cavity stable. For this reason the optimum number of bunches depends on the shape of the ring. In Fig. 30 two examples are given. As the ring is more circular, the straight sections, and hence the undulator length, will be relatively short. A multi-bunch mode is then advantageous since it reduces the intra-bunch distance to reduce the cavity length. The combination of the short cavity with a single-bunch mode is not advantageous since the optical pulse then has to pass the cavity twice before encountering interaction with the electron bunch. Hence, the effective cavity loss is doubled.

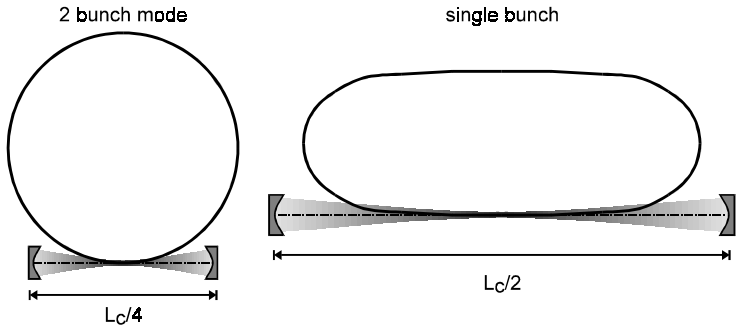

Fig. 30 Ring geometries

For the SRFEL it is advantageous to shorten the circumference of the ring while maximising the undulator length. The racetrack design, depicted in the left-hand side of Fig. 30 is, therefore, advantageous. Dedicated rings such as the one at Duke in Durham, North Carolina and DELTA in Dortmund both have this design and are designed to run in a single-bunch mode.

5.2 Beam current and electron beam quality

The most straightforward method to increase the peak current is to simply increase the average current in the ring. However, as the average beam current goes up some undesired effects need to be considered. Two aspects are of special importance: the lifetime of the beam and current-induced instabilities.

The Touschek effect

For electron beams with a high volume density the Touschek effect plays a significant role. This is the process whereby, due to Coulomb scattering within a single beam bunch the transverse-to-longitudinal momentum exchange can lead to loss of longitudinal stability, if the (energy) variation exceeds the magnitude of the energy acceptance of the longitudinal phase-stable domain [55]. The Touschek lifetime is proportional to:

$$\tau_{\text{tou}} \propto \gamma^3 \frac{I_p}{\sigma_x \sigma_y} \tag{45}$$

A long beam lifetime is important because of the long-time (thermal) effects that take place. For example thermal effects on the mirrors of the FEL, see Sec. 4. To maximise lifetime several options are available:

- An optimum choice of the emittance: Modern storage rings can have a very small emittance, down to a few nm in the horizontal plane. Depending on the spectral domain of interest this can be lower than that required for proper FEL operation, see Eq. (8) and Eq. (18).
- A full coupling of the horizontal and vertical emittance of the ring, e.g. by installing a skewed quadrupole. The coupling results in a larger phase-space and, hence, a longer Touschek lifetime. The FEL gain will, most probably, not change too much. Note that this is not a general rule, however. For specific cases it is necessary to consider the impact on the FEL gain as seen in Eq. (8) and Eq. (18).
- An increase in the longitudinal phase-stable domain of the ring, i.e. an increase of the rf-power employed. This is also advantageous since the saturation process of the FEL can increase the energy spread in the ring.
- An increase of the beam energy. The Touschek lifetime increases with increasing beam energy. An additional advantage is the increases saturated power level of the laser, see Eqs. (23) and (24). Due to this the radiation flux on the mirrors increases as well, however, firstly because of the increased synchrotron power, Eq. (24) and secondly because of the increase in harmonics: as the beam energy increases the undulator strength must increase as well to keep the radiated wavelength constant. The higher magnetic field strength causes a significant increase in harmonics, Fig. 38.

Current-induced effects

As the beam circulates in the ring the electromagnetic field of a bunch is coupled with the impedance of the environment (discontinuity of the vacuum chamber, rf cavity, etc.) to the same bunch [55, 56]. This effect becomes more important as the intensity, i.e. the average beam current in the ring, increases. The stationary solution gives the so-called “potential-well” distortion at rather low current. At higher currents one reaches the threshold of anomalous bunch lengthening. At Super ACO, for example, this threshold is found to be at approximately 8 mA/bunch [57]. Above this limit the so-called “microwave instability regime” is entered. In addition, the bunch or bunches can also start to oscillate coherently close to their natural oscillation synchrotron frequency and its harmonics. The presence of modes of oscillations (dipolar, quadrupolar, hexapolar and octupolar) depends on the beam current. In the upper limit of the current the beam becomes completely unstable. At Super ACO this limit is reached at roughly 100 mA/bunch [33].

For the FEL it is clear that the laser would work best in the absence of any type of instability. However, as a general rule the FEL operates in a regime where the instabilities are present. For example at Super ACO the under-threshold for lasing is reached at roughly 15 mA/bunch, far above the threshold for anomalous bunch lengthening. Here it is important to note that not all instabilities are of the same importance.

(a) *Coherent bunch-oscillations.* In Fig. 31 the coherent synchrotron modes of oscillation, as observed at Super ACO, are shown. As can be deduced from the left-hand side of the figure these types of modes are devastating for the FEL: from the plot of the line-intensity it follows that the position of the bunch starts to oscillate. Hence, the effective small-signal gain is reduced since, over multiple roundtrips, the effective longitudinal overlap of the bunch with the optical pulse is reduced. Next it can be seen that also the effective energy-spread increases, causing a further decrease

of the small-signal gain. At Super ACO the dipolar modes are damped with a Pedersen type of feedback system [58, 59]. With this system it is possible to obtain stable operation up to a current of 35 mA/bunch. Above this threshold quadrupolar modes occur that make the start-up of the laser more difficult. Moreover, with quadrupolar modes present the laser becomes less stable. However, once lasing is achieved, the FEL interaction tends to damp these modes [33]. Recently, feedback on the quadrupolar modes has been installed providing the means to have stable FEL operation at up to 50 mA/bunch [60].

(b) *Microwave instability*. At higher circulating beam current in a storage ring significant dilution of longitudinal phase-space density may occur. Here the interaction of the bunch with its own short-range wake field causes high-order coupled oscillatory modes to be induced. This results in short-wavelength (compared with the bunch length) particle density modulation of the bunch, effective lengthening of the bunch, and enhancement of the energy spread. The threshold peak current for the longitudinal single-bunch instability is given by [23]:

$$I_p = 2\pi\alpha\left(\frac{\sigma_\gamma}{\gamma}\right)^2 \frac{(E_0/e)}{(Z_\parallel/n)} \tag{46}$$

where E_0 and $Z_\parallel$ are the beam energy and the longitudinal impedance of the ring, respectively. Above the threshold the peak current may still increase but at the expense of an increase in energy spread [23]:

$$\frac{\sigma_\gamma}{\gamma} = \sqrt[3]{\frac{1}{2\pi}\frac{\nu_s I_0}{\alpha^2 (E_0/e)^2 h}\frac{(Z_\parallel/n)}{}}$$
$$\nu_s \approx \sqrt{\frac{V_{\mathrm{rf}}\, h\alpha}{2\pi E}} \tag{47}$$

where I_0 is the average beam current, V_{rf} is the rf voltage, and h is the number of bunches stored in the ring.

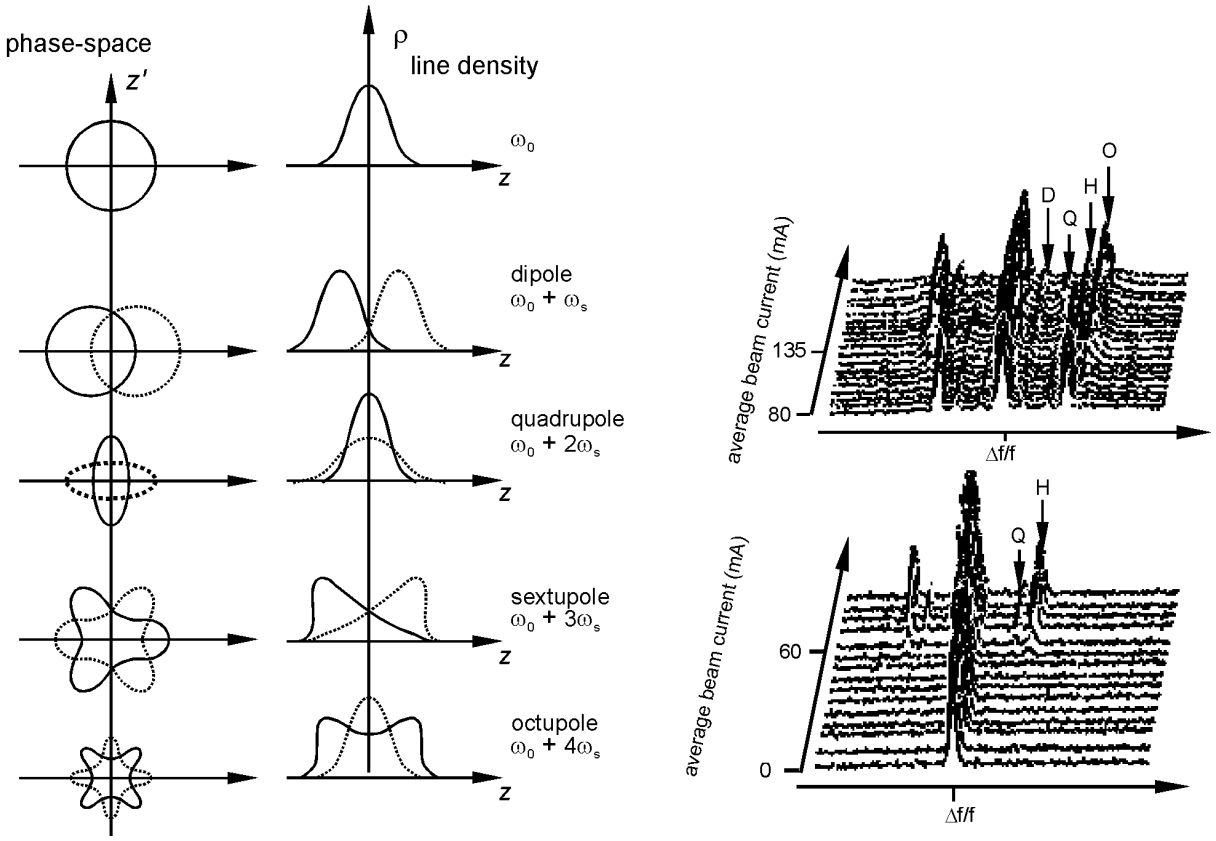

Fig. 31 Synchrotron modes of oscillations observed at Super ACO in a two-bunch mode of operation [33]. Left-hand side: Representation of the coherent synchrotron modes of oscillation in phase space and in time space. Right-hand side: Spectrum of the modes observed on the sidebands of high harmonics of the revolution frequency versus the stored beam current. With increasing current one can observe the presence of dipolar modes (D), quadrupolar modes (Q) hexapolar modes (H) , and octupolar modes (O).

To first order the gain of the laser scales with the square of the energy spread. Hence, even at the occurrence of microwave instability, it remains worthwhile to increase the beam current. Nevertheless, it is also important to design the storage ring such that instabilities are avoided to an as high as possible current. To do so it is important to reduce the number of bunches in the ring, see Sec. 5.1. Increasing the rf voltage also helps but is not very effective, see Eq. (47). A high rf voltage remains important, however, since it also determines the energy-spread acceptance of the ring, see Sec. 3.

In the optimisation process the momentum compaction factor α plays an important role: as the compaction factor becomes smaller the storage ring becomes more sensitive to instabilities. Hence, a too small value for α is to be avoided. However, big compaction factors are non-ideal either. From Eq. (3.2) it follows that a small value for α leads to short bunches and, hence, to high peak currents and gain. Furthermore, there is a (indirect) relation between the compaction factor and the emittance since both are related to the so-called “synchrotron radiation integrals” [23]:

$$\alpha = \frac{I_1}{R}$$
$$\varepsilon_x = \frac{55}{32\sqrt{3}} \frac{\hbar}{mc} \gamma^2 \frac{I_5}{I_2 - I_4} \tag{48}$$

where the synchrotron integrals are given by:

$$I_1 = \int_{\text{dipoles}} \frac{\eta}{\rho} ds, \qquad I_2 = \int_{\text{dipoles}} \frac{1}{\rho^2} ds, \qquad I_3 = \int_{\text{dipoles}} \frac{1}{|\rho^3|} ds$$
$$I_4 = \int_{\text{dipoles}} \frac{(1-2n_d)\eta}{\rho^3} ds, \qquad I_5 = \int_{\text{dipoles}} \frac{H}{|\rho^3|} ds \tag{49}$$

with:

$$H = \gamma_x \eta_x^2 + 2\alpha_x \eta_x \eta'_x + \beta_x \eta'^2_x \qquad \text{dispersive invariant}$$
$$\mathrm{n_d} = \frac{r}{B}\frac{\partial B}{\partial r} \qquad \text{dipole magnetic field index} \tag{50}$$

and $\eta = \eta(s)$ the dispersion function. The parameters $\alpha_x(s)$, $\beta_x(s)$, $\gamma_x(s)$ are the machine Twiss coefficients. Note that the differentiation is with respect to *s*, the lattice azimuthal coordinate, and integration is over the extent of the dipole regions only.

From Eqs. (48) and (49) it follows that a careful optimisation of the dispersion is necessary: small dispersions lead to a small emittance and, through the compaction factor, to short bunches and a high peak-current. However, a too small compaction factor causes more instability. In modern machines it is feasible to reduce the emittance to only a few nm. Normally this goes in parallel with a decrease in α. For the FEL it might be advantageous to tune the compaction factor independent of the emittance, e.g. by adding additional dispersive elements in a straight section of the ring. It might thus be possible to operate the ring at any (positive or negative) value of the compaction factor. At present only A few storage rings have the possibility to change α and more studies are required to find an optimum. A study at Super ACO [57] indicates that a negative compaction factor might be advantageous: running with negative α resulted in shorter bunches but higher energy spread. With more tuning it might thus be possible to find optimum conditions for FEL operation in a storage ring.

The most promising option would be to run a ring at $\alpha = 0$. This situation is known as the isochroneous SRFEL [61]. In normal SRFEL operation the micro bunching on the scale of the wavelength, a process that occurs naturally as the electrons pass through the undulator, is lost as the electrons make their turn through the ring. If the compaction factor would be sufficiently small, however, this bunching could be maintained on successive turns through the ring. The advantages are obvious since an already bunched beam would start radiating coherently directly when entering the undulator. Hence, the gain would be increased by orders of magnitude. At present no storage ring has demonstrated this, however. The main reason is the small compaction factors required. For example, lasing at 500 nm in a small ring with a circumference of 50 m would already require $|\alpha|<10^{-6}$. It might be possible to demonstrate the effect in the (far) infrared in a small, low-energy ring, however.

5.3 Machine functions

In Sec. 4.1 the average transverse optical mode area was minimised for the case of a standard two-mirror resonator. Here this process is repeated for the electron beam. Since the transverse mode area of the electron beam is generally less than the optical mode area (from Eq. (8) it follows that $\varepsilon_x\varepsilon_y << \lambda^2$) this process is less important. Nevertheless this optimisation is a useful exercise. An example of such an optimisation is shown in Fig. 32. In the figure the

gain of the Super ACO FEL is plotted as a function of the horizontal Twiss parameter β_x. The results are based on the model presented in Appendix B.

From the figure it follows that an optimum gain is obtained for a β_x in the range from 4 to 7 m, depending on the resonator geometry, i.e. the Raleigh length β_0. Most important for a proper optimisation is the matching of the curvature of the phase-front of both the optical wave and of the electron beam. Hence, in the case of a shorter Raleigh-length the Twiss parameters β_x and β_y need to be reduced as well. The figure also shows that the gain is fairly insensitive for moderate increases of the transverse beam size. For Super ACO ($\beta_0 \approx 3$ m) an optimum gain of 2 % is reached for $\beta_x \approx 5$ m. For reasons concerning the stability of the optical resonator, see Sec. 4.1, this is somewhat lower than the maximally achievable gain when $\beta_0 = 1.5$ m and $\beta_x = \beta_y = 4$ m.

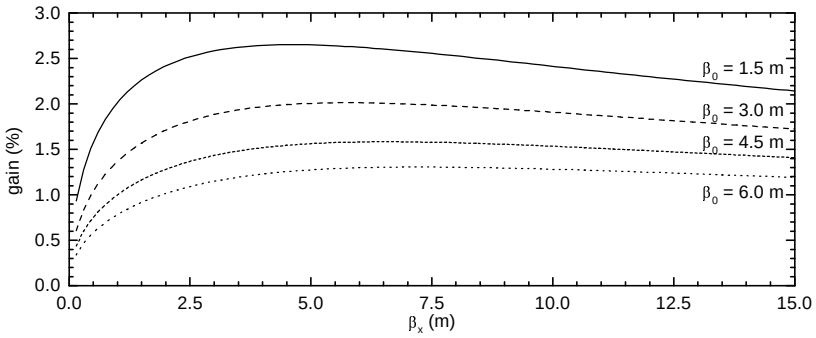

Fig. 32 The gain of Super ACO as a function of the machine Twiss parameter β_x in the centre of the undulator for several values of the Raleigh-length of the resonator. For Super ACO ($\beta_0 \approx 3$ m) the optimum gain is reached for $\beta_x \approx 5$ m.

REFERENCES

[1] M. Billardon, P. Elleaume, J.M. Ortéga, C. Bazin, M. Bergher, M. Velghe, Y. Petroff, D.A. Deacon, K.E. Robinson, J.M.J. Madey, Phys. Rev. Lett. **51**, 1652 (1983)

[2] N.A. Vinokurov, V. Litvinenko, Proc. of the SR88 Conf., Novosibirsk, Nucl. Instr. Meth. **A282**, 424 (1989)

[3] H. Hama, J. Yamazaki, G. Isoyama, Nucl. Instr. Meth. **A341**, 12 (1994)

[4] M.E. Couprie, M. Billardon, M. Velghe, C. Bazin, J.M. Ortega, R. Prazeres, Y. Petroff, Nucl. Instr. Meth. **A296**, 13 (1990)

[5] V.N. Litvinenko, B. Burnham J.M.J. Madey, S.H. Part, Y. Wu, Nucl. Instr. Meth. **A375**, 46 (1996)

[6] D. Nölle and the DELTA group, Nucl. Instr. Meth. **A375**, ABS48 (1996)

[7] K. Hayakawa, T. Tanaka, Y. Torizuka, K. Sato, Y. Matsubara, I. Kawakami, I. Sato, S. Fukuda, S. Anami, T. Kurihara, T. Kamitani, T. Ohsawa, A. Enomoto, S. Toyama, M. Nomura, Y. Yamazaki, T. Yamazaki, K. Yamada, M. Ikezawa, Y. Sibata, M. Oyamada, Nucl. Instr. Meth, **A375**, ABS25 (1996)

[8] T. Yamazaki, K. Yamada, S. Sugiyama, H. Ohgaki, N. Sei, T. Mikado, T. Noguschi, M. Chiwaki, R. Suzuki, M. Kawai, M. Yokoyama, K. Owaki, S. Hamada, K. Aizawa, Y. Oku, A. Iwata, M. Yoshiwa, Nucl Instr. Meth. **A331**, 27 (1993)

[9] M.P. Level, P. Brunelle, M. Corlier, G. Flynn, C. Herbeaux, A. Nadji, J. Neel, P. Nghiem, J. Payet, P. Peaupardin, J.P. Pénicaud, M. Sommer, A. Tkatchenko, M. Tkatchenko, Proc. of the 5th Eur. Part. Accel. Conf. (EPAC), Sitges Spain, (1996)
[10] K. Yamada, T. Yamazaki, S. Sugiyama, H. Ohgaki, T. Noguchi, T. Midado, M. Chiwaki, R. Suzuki, T. Tomimasu, Nucl. Instr. Meth., **A331**, 103 (1993)
[11] M.E. Couprie, R.J. Bakker, D. Garzella, L. Nahon, M. Marshi, F. Mélora, T. Hara, M. Billardon, Nucl. Instr. Meth., **A375**, 639 (1996)
[12] Free Electron Lasers and other advancd sources of light, Report by the Board on Chemical Sciences and Technology, National Resarch Council, Washington D.C., USA (1994)
[13] Proc. of the ICFA workshop on 4th generation light sources, Jan 1994, Grenoble, France
[14] J.M.J. Madey, Il Nuovo Cim. **50B**, 64 (1979)
[15] G. Dattoli and A. Renieri, *Laser Handbook Vol. 4*, Eds. M.L. Stitch and M. Bass, North Holland Publ., Amsterdam, p. 1-142 (1985)
[16] C.A. Brau, *Free Electron Lasers*, Academic Press, Boston (1990)
[17] A. Cutolo, S. Solimento, Appl. Opt., **26**, 53 (1987)
[18] N.A. Vinokurov, Proc. 10th Int. Conf. on High Energy Charged Particle Accelerators, **2**, Serpukhov, p. 454 (1977)
[19] R.H. Pantell, L.K. Grover, *Laser Handbook Vol. 6*, Eds. W.B. Colson, C. Pellegrini, R. Renieri, North Holland Publ., Amsterdam, p. 71-90 (1990)
[20] P. Elleaume, *Laser Handbook Vol. 6*, Eds. W.B. Colson, C. Pellegrini, R. Renieri, North Holland Publ., Amsterdam, p. 91-114 (1990)
[21] D.A.G. Deacon, J.M. Ortega, *Laser Handbook Vol. 6*, Eds. W.B. Colson, C. Pellegrini, R. Renieri, North Holland Publ., Amsterdam, p. 71-90 (1990)
[22] M. Sands, Stanford Linear Accelerator Centre, Report 121, (1970)
[23] A. van Steenbergen , *Laser Handbook Vol. 6*, Eds. W.B. Colson, C. Pellegrini, R. Renieri, North Holland Publ., Amsterdam, p. 417-462 (1990)
[24] H. Hama, K. Kimura, T. Yamazaki, S. Tanako, K. T. Kinochita, M.E. Couprie, Nucl. Instr. Meth., **A375**, 32 (1996)
[25] A. Renieri, Nuovo Cimento, **53B**, p. 160 (1979)
[26] *The synchrotron light source data book*, eds. J. Murphy, BNL 42333, NSLS 725C, P.O. Box 5000, Upton New York 11973-5000, (1993)
[27] P. Elleaume, Nucl. Instr. Meth., **A237**, 28 (1985)
[28] M.E. Couprie, N.G. Gavrilov, G.N. Kulipanov, V.N. Litvinenko, I.V. Pinaev, V.M. Popik, A.N. Strinsky, N.A. Vinokurov, Nucl. Instr. Meth, **A304**, p. 47 (1991)
[29] T. Hara, M.E. Couprie, A. Delboulbé, L. Nahon, M. Billardon, Nucl. Instr. Meth. **A358**, 341 (1995)
[30] M.E. Couprie, D. Garzella, T. Hara, J.H. Codarbox, M. Billardon, Nucl. Instr. Meth, **A358**, p. 374 (1995)
[31] P. Elleaume, J. Phys., **45**, 997 (1984)
[32] T. Hara, M.E. Couprie, M. Billardon, Nucl. Instr. Meth. **A375**, 67 (1996)
[33] M.E. Couprie, T. Hara, D. Gontier, P. Troussel, D. Garzella, A. Delboulbé, M. Billardon, Phys. Rev. E, **53-2**, 1871 (1996)
[34] M. Billardon, P. Elleaume, J.M. Ortega, C. Bazin, M. Bergher, Y. Petroff, M. Velghe, Nucl. Instr. Meth., A237, 244 (1985)
[35] W.B. Colson, *Laser Handbook Vol. 6*, Eds. W.B. Colson, C. Pellegrini, R. Renieri, North Holland Publ., Amsterdam, p. 115-194 (1990)
[36] A.E. Siegman, *Lases*, Universiyt Science Books, Mill Valley (CA), USA

[37] A. Yariv, *Introduction to Optical Electronics*, Holt, Rinehart and Winston, New York 1971, pp. 61
[38] W. Dricsoll, W. Vaugham eds., *Handbook of Optics*, Mc Graw-Hill Book Company, New York, USA
[39] W.L. Wolfe, G.J. Zissis, *The Infra-red Handbook*, Ofice of Naval Research, Dep. of the Navy, Washington D.C., USA (1985)
[40] D.T. Attwood et al, AIP CONF. Proc. **118**, eds J.M.J. Madey and C. Pelligrini, AIP, New York, p. 93 (1983)
[41] H.E. Bennet, D.K. Burge, J. opt. Soc. Am., **70**, 268 (1980)
[42] M. Billardon, P. Ellaume, J.M. Ortega, C. Bazin, M. Bergher, M.E. Couprie, Y. Lapieree, Y. Petroff, R. Prazeres, M. Velghe, Nucl. Instr. Meth. **A259**, 72 (1987)
[43] S.M. Edlou, A. Smajkiewicz, A. Ghanim, A-Jumaily, Appl. Opt., **32**, 5601 (1993)
[44] D. Garzella, Etude d'un Laser a Electrons Libres dans l'ultra-violet sur l'anneau de stocage Super ACO, thesis of the univ. de Paris IX, Orsay, 153 (1996)
[45] J.M. Elson, J.M. Bennett, J. Opt Soc. Am., **69**, 31 (1979)
[46] D. Garzella, M.E. Couprie, T. Hara, L. Nahon, M. Brazuna, A. Delboulbé, M. Billardon, Nucl. Instr. Meth, **A358**, 387 (1995)
[47] M.E. Couprie, D. Garzella, M. Billardon, Nucl. Instr. Meth, **A358**, p. 382 (1995)
[48] K. Yamada, T. Ymazaki, N. Sci, T. Mikado, Nucl. Instr. Meth, **A341**, ABS139 (1994)
[49] H. Hama, Nucl. Instr. Meth, **A375**, 57 (1996)
[50] C. Shih, S. Shih, Nucl. Instr. Meth, **A304**, 788 (1991)
[51] D.H. Dowell, M.L. Laucks, A.R. Lowrey, J. Adamski, D. Pistoresi, R. Shoffstall, A.H. Lumpkin, S. Bender, D. Byrd, R.L. Tokar, K. Sun, M. Bentz, R. Burns, J. Guha, W. Tomita, Nucl. Instr. Meth, **A318**, 74 (1992)
[52] B.E. Newnam, SPIE, **738**, Free-Electron Lasers, 155 (1987)
[53] B. Gerard, Y. Lapierre, J.M. Ortega, C. Bazin, M. Billardon, P. Elleaume, M. Ergher, M. Velghe, Y. Pertroff, Phys. Rev. Lett, **53**, 2405 (1984)
[54] R. Prazeres, J.M. Ortega, Europhys. Lett, **4**, 817 (1987)
[55] J.L. Laclare, Bunched Beam Instabilities (F.J. Sacherer Memorial Paper) Proc. 11th Int. Conf. On High Energy Accelerators, p 526
[56] J.L. Laclare, CERN Report No. 264-326, 1987
[57] R.J. Bakker, M.E. Couprie, L. Nahon, D. Nutarelli, R. Roux, A. Deboulbé, D. Garzella, A. Nadji, B. Visentin, M. Billardon, Proc. of the 5th Eur. Particle Accelerator Conference (EPAC) , Sitges, Spain, 667 (1996)
[58] F. Pedersen, F. Sacherer, IEEE Trans. Uncl. Sci., **NS-24**, 1396; B. Kriegbaum, F. Pedersen, IEEE Trans. Nucl. Sci., **NS-24**, 1695 (1977)
[59] M.E. Couprie, M. Billardon, IEEE J. of Quan. El., **30-3**, 781 (1994)
[60] R. Roux, M.E. Couprie, T. Hara, R.J. Bakker, A.B. Visentin, M. Billardon, J. Roux, Nucl. Instr. Meth., **A393**, 33 (1997)
[61] D.A.G. Deacon, Phys. Rep. **76**, 351
[62] Super ACO Parameter List, Super ACO/87-38, Orsay, France (1987)
[63] E.I. Zinine, Nucl. Instr. Meth., **A208**, 439 (1983)

APPENDIX A

THE SUPER ACO FEL

In this chapter the free-electron laser installed in the synchrotron light source Super ACO [7, 62] takes a special place. Together with the ACO FEL this facility has the longest history of operation. Moreover, the author of this chapter is most familiar with this SRFEL. Consequently a major part of the operational examples presented here originate from these facilities.

An overview of the machine is given in Fig. A.1 and its parameters are given in Table A.1. A full energy positron linac injects the particles into an octagon-shaped ring with a circumference of 72 m. For FEL operation the ring is filled with two identical, equidistant bunches with a maximum current of 45 mA/bunch, i.e. up to 20 A of peak current. A 2-times-10-period optical klystron in a dispersive free section of the ring forms the centre of the laser. The OK is enclosed in an 18-m long optical resonator. Light is coupled out through the multi-coated mirrors at both sides of the undulator. The south-mirror can move along the axis of the resonator to synchronize the length of the cavity to half the bunch distance. Tuning the frequency of the 100-MHz rf cavity achieves fine tuning of the bunch distance, see Sec. 3.3.

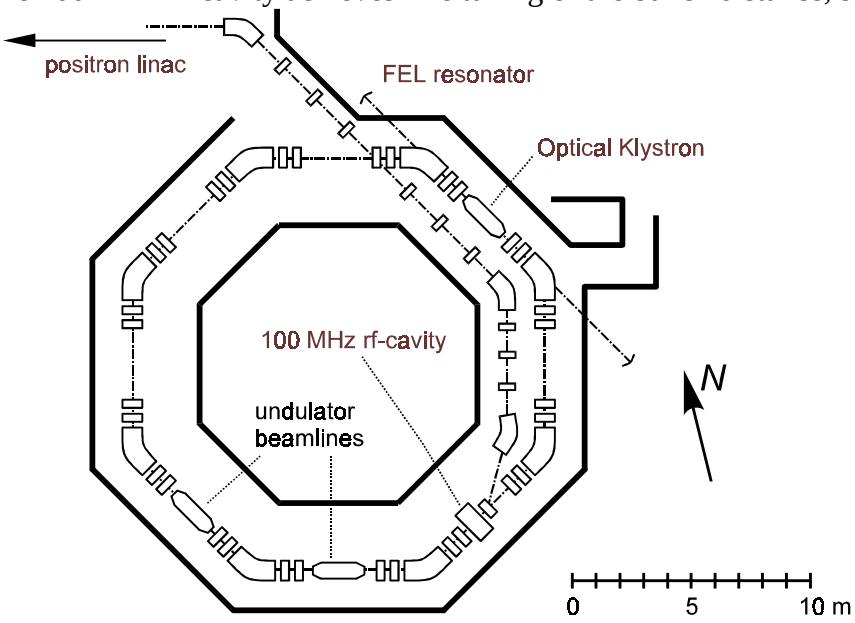

Fig. A.1 Layout of Super ACO

During a typical week the synchrotron provides 113 hours of operation (including injection time) of which an average of 21.5 hours are dedicated to FEL operation. The parameters of the laser are chosen to be compatible with a standard two-bunch mode of operation at the default beam energy of Super ACO of 800 MeV. The main differences are the reduced beam current and the slightly altered machine functions in the straight section of the OK. The former is necessary to avoid beam-instability, see Sec. 5.2. The latter enables an optimisation of the gain, see Sec. 5.3. Since this is a minor adjustment, laser operation can take place in parallel with the use of synchrotron beam lines. As such the FEL can also be considered as just an advanced beam line. Moreover, it is possible to perform experiments where, in a single experiment, the output of the FEL is used in combination with the output of a second (undulator) beam line. This way it is possible to do two-color pump-probe

experiments with a repetition rate of 8.3 MHz. At Super ACO roughly 50 % of the FEL beam time is used for this and other types of user experiments [11].

Table A.1

Super ACO parameters

Beam Energy	E	600-800	MeV
Circumference	L_c	72	m
Momentum compaction factor	α	0.0148	
rf-frequency	f_{rf}	100	MHz
Number of bunches		2	
Max. average beam current	I_a	200	mA
Damping time	τ_s	10-20	ms
Synchrotron frequency	f_s	14-17	kHz
Beam life time	τ	6	hours
Energy spread	σ_γ/γ	0.065	%
Emittance	$\varepsilon_{x,y}$	20	π nm rad
Transverse beam size	$\sigma_{x,y}$	0.3	μm
Transverse machine functions in OK	$\beta_{x,y}$	5	m
Energy dispersion in OK	$\eta_{x,y}$	0	
Cavity length	L	18	m
Maximum undulator strength	K	3.9	
Undulator period	λ_u	12.9	cm
Number of periods	N	2x10	
Strength dispersive section	$N+N_d$	<120	
Wavelength range	λ	600-350	nm
Laser gain	G_0	2	%
Average output power	P	100	mW
Micro-pulse duration	σ_t	12	ps
Spectral width	$\Delta\lambda/\lambda$	10^{-4}	

Two types of temporal diagnostic are presented in Fig. A.2 and Fig. A.3: a double-sweep streak-camera and a dissector. With a dissector (synchrotron or laser) light is projected onto a pinhole with a photo-cathode. The intensity evolution on the pinhole is then transformed into a spatial distribution with a fast transverse sweep on two deflecting electrons that deflect the passing electron beam. Behind the anode a fluorescent screen makes it possible to display the distribution on a photo or CCD camera. With a double-sweep camera an additional synchronised slow sweep is applied perpendicularly to the fast sweep. This way it is possible to record the evolution of a repeating signal, e.g., an electron bunch providing synchrotron radiation at a dipole beam line on each turn through the ring. The image in Fig. A.2 is a recording of the Super ACO FEL pulse in a pulsed mode of operation, i.e. zone ±1 in Fig. 23. The streak-camera at Super ACO (Hamamatsu C5680) has a resolution of a few ps. The slow sweep can be set in a range from 100 ns to 1 s.

A dissector, developed at Novosibirsk [63], is in fact identical to a streak camera equipped with a single-pixel CDD camera. The temporal information can now be obtained in a stroboscopic way, i.e. by applying a slowly varying bias voltage to the fast sweep of the deflecting electrodes. The temporal resolution of the dissector at Super ACO is of the order of 10 ps. The main advantage of a dissector is its capability to process its signal directly by means of an oscilloscope or other electronic equipment, e.g. the feedback system described in Sec. 3.3. Due to its stroboscopic nature it is not possible to follow fast changing phenomena

such as the synchrotron modes of oscillation described in Sec. 5.2. Furthermore, it can only be used to record periodic events.

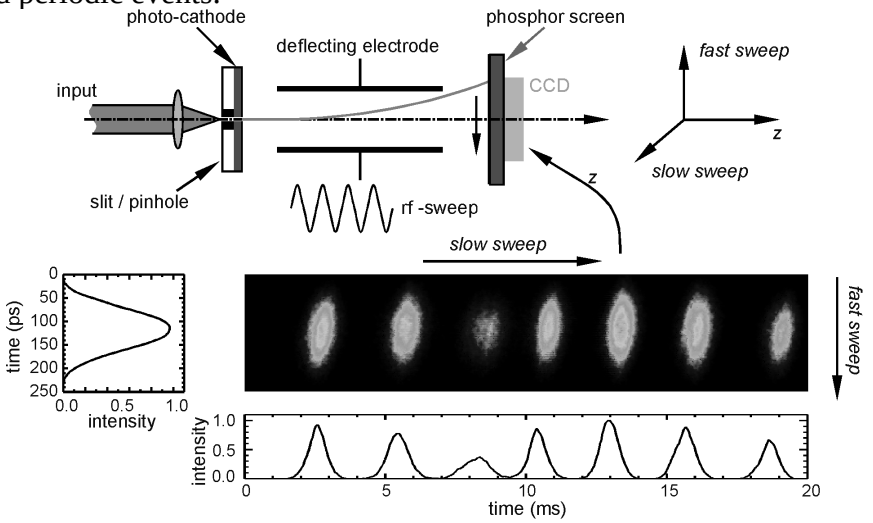

Fig. A.2 Schematic view of a double-sweep streak-camera. The lower image shows the pulsed output of the Super ACO FEL.

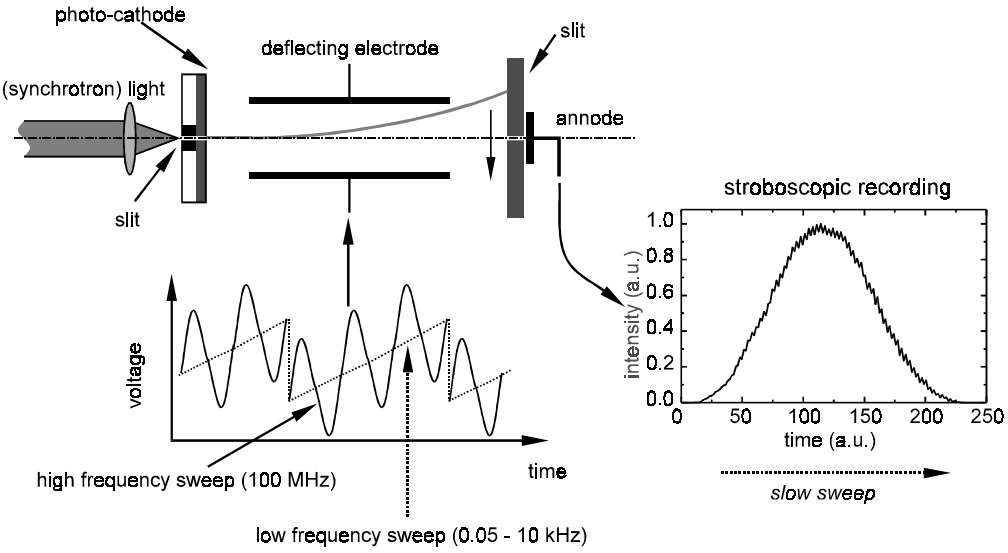

Fig. A.3 Schematic view of a dissector. The image shows a stroboscopic recording of the laser output at low intensity, i.e. zone 2 in Fig. 12.

APPENDIX B

3D SEMI-ANALYTICAL GAIN CALCULATIONS

In the following a formula for the gain for an FEL and optical klystron is derived[*•], including 3D effects, i.e. transverse interaction with the optical mode, emittance, and energy spread. Within this context the following assumptions are used:

- A continuous electron beam, i.e. the slippage effect is neglected.
- Operation in the small-signal, low-gain regime, i.e. the slowly varying amplitude and phase approximation.
- Interaction with a Gaussian TEM_{00} transverse optical mode (not a fundamental restriction).
- Interaction with an electron beam with an arbitrary Gaussian distribution in phase space.

To derive the equation this Appendix has been divided into four sections. Section B1 serves as an introduction. In this section the well-known 1D gain formula for a regular FEL where an ideal electron beam interacts with a plane wave has been derived. In Sec. B2 the gain formula is modified to describe the effect of energy spread on the electron beam. This section serves as a simple example for Sec. B3 where all the above-mentioned 3D effects are included in the gain formula. In Sec. B4 the modifications required to describe an OK are discussed.

B.1 Gain calculation for an ideal beam

In this section a plane wave with angular frequency ω and a wave vector k, propagating in z direction is assumed. For this wave the electric field looks like:

$$\begin{aligned} E_x &= E_0 \Re\left(e^{i(\omega t - kz + \phi)}\right) \\ &= E_0 \cos(\omega t - kz + \phi) \end{aligned} \tag{B1}$$

where ϕ denotes an arbitrary phase of the field. An electron, with a velocity component parallel to the electric field will experience a force $-eE$ and, hence, will gain or lose kinetic energy. The energy change for an individual electron with energy γmc^2 can be expressed as

$$d\gamma = -\frac{e}{mc^2} E_x(z,t)\, dx \tag{B2}$$

where γ is the Lorentz factor, m the electron rest mass, c the vacuum velocity of light, and e the electron charge. Integration of Eq. (B2) leads to

$$\begin{aligned} \Delta\gamma(z) &= -\frac{e}{mc^2} \int_{z_i}^{z} E_x(z_1,t) \frac{dx}{dz} dz_1 \\ &= -\frac{e}{mc^2} \int_{z_i}^{z} E_x(z_1,t) x' dz_1 \end{aligned} \tag{B3}$$

When bunching of the electrons is expressed as a deviation in arrival time (t_0) at a given position z, the energy deviation can be expressed as a Taylor expansion around t_0

[*•]Calculations have been taken from the thesis of V. Litvinenko: "VEPP-3 Storage Ring Optical Klystron: Lasing in the Visible an the UV" Dissertation of the Institute of Nuclear Physics, Novosibirsk, 1989

$$\begin{aligned}\Delta\gamma(z) &= \Delta\gamma_1(z) + \Delta\gamma_2(z) + \cdots \\ &= -\frac{e}{mc^2}\int_{z_i}^{z} E_x(z_1,t_0)x'(z_1)dz_1 - \frac{e}{mc^2}\int_{z_i}^{z} E_x(z_1,t_0+\Delta t)x'(z_1)dz_1 + \cdots\end{aligned} \tag{B4}$$

The first term $\Delta\gamma_1$ describes the FEL interaction without bunching. In this case there is no net energy loss for a distribution of electrons within one ponderomotive well, hence

$$\left\langle \Delta\gamma_1(z)\right\rangle_\lambda = 0 \tag{B5}$$

The second term, $\Delta\gamma_2$, describes the effects of bunching. For this the time deviation can be expressed as a phase-fluctuation with $\Delta\phi = -\omega\Delta t$. Hence, $\Delta\gamma_2$ can be expressed as

$$\Delta\gamma_2 = \frac{e}{mc^2}\int_{z_i}^{z}\frac{dE_x(z_1,t_0+\Delta t)}{d\phi}\Delta\phi(z_1)x'(z_1)dz_1 \tag{B6}$$

where $\Delta\phi(z_1)$ is a function of the dispersion D in the undulator

$$\begin{aligned}\Delta\phi(z) &= \int_{z_i}^{z}\Delta\gamma(z_1)\int_{z_i}^{z_1}E_x(z_2)x'(z_2)dz_2\,dz_1 \\ &= \frac{e}{mc^2}\int_{z_i}^{z}E_x(z_2)x'(z_2)\int_{z_i}^{z_1}D_z(z_1)dz_2\,dz_1 \\ &= \frac{e}{mc^2}\int_{z_i}^{z}E_x(z_2)x'(z_2)D_z(z_2,z)dz_2\,dz_1\end{aligned} \tag{B7}$$

For a planar undulator $D(z_2,z_1)$ reads

$$D(z_1,z_2) = \frac{2k_u}{\gamma}(z_1 - z_2) \tag{B8}$$

A combination of Eqs. (B6) and (B7) leads to

$$\Delta\gamma_2 = -\left(\frac{e}{mc^2}\right)^2\int_{z_i}^{z_f}\int_{z_i}^{z_1}\frac{dE_x(z_1,t_0+\Delta t)}{d\phi}x'(z_1)E_x(z_2)x'(z_2)D(z_1,z_2)dz_2\,dz_1 \tag{B9}$$

The average energy lost per electron over one ponderomotive well thus becomes

$$\left\langle\Delta\gamma_2\right\rangle_\lambda = -\left(\frac{e}{mc^2}\right)^2\int_{z_i}^{z_f}\int_{z_i}^{z_1}\left\langle\frac{dE_x(z_1,t_0+\Delta t)}{d\phi}x'(z_1)\right\rangle_\lambda\left\langle E_x(z_2)x'(z_2)\right\rangle_\lambda D(z_1,z_2)dz_2\,dz_1 \tag{B10}$$

For an FEL with a planar undulator the terms in Eq. (B10) can be expressed as

$$\begin{aligned}\left\langle E_x(z_2)x'(z_2)\right\rangle_\lambda &= E_0\frac{K}{\gamma}\left\langle\cos(\omega t - kz + \phi)\sin(k_u z)\right\rangle_\lambda \\ &= E_0\frac{K}{2\gamma}\left(J_0(\xi) - J_1(\xi)\right)\cos(\delta kz + \phi)\end{aligned} \tag{B11}$$

where $J_{0,1}$ represent the Bessel functions of the first kind. K and δk are the undulator strength and the detuning parameter, respectively.

$$K = \frac{eB_u\lambda_u}{2\pi mc}$$
$$\xi = \frac{K^2}{4+2K^2} \tag{B12}$$
$$\delta k = k - 2k_u\gamma^2$$

Combination of Eqs. (B10) and (B11) leads to an average energy loss (averaged over one wavelength)

$$\begin{aligned}\Delta\gamma_2 &= -\frac{1}{4}\left(\frac{e}{mc^2}\right)^2\left(\frac{K}{\gamma}\right)^2\left(J_0(\xi)-J_1(\xi)\right)^2E_0^2 \\ &\qquad \int_{z_i}^{z_f}\int_{z_i}^{z_1}\cos(\delta k z_1+\phi)\cdot\cos(\delta k z_2+\phi)D(z_1,z_2)dz_2\,dz_1 \qquad \text{(B13)}\\ &= -\frac{1}{8}\left(\frac{e}{mc^2}\right)^2\left(\frac{K}{\gamma}\right)^2\left(J_0(\xi)-J_1(\xi)\right)^2E_0^2\int_{z_i}^{z_f}\int_{z_i}^{z_1}\sin\left(q(z_1-z_2)\right)D(z_1,z_2)dz_2\,dz_1\end{aligned}$$

The integral can be made dimensionless by rescaling the whole integral over the total interaction length $L = z_f - z_i$. The expression above then becomes

$$\Delta\gamma_2 = -\frac{1}{8}\left(\frac{e}{mc^2}\right)^2\left(\frac{KL}{\gamma}\right)^2\left(J_0(\xi)-J_1(\xi)\right)^2E_0^2\int_{-\frac{1}{2}}^{\frac{1}{2}}\int_{-\frac{1}{2}}^{z_1}\sin\left(q(z_1-z_2)\right)D(z_1,z_2)dz_2\,dz_1 \tag{B14}$$

where δk has been substituted with $q = L\,\delta k$. Also the dispersion D has been normalised with respect to the interaction length. Eq. (B8) thus becomes

$$D(z_1,z_2) = \frac{4\pi L}{\lambda_u\gamma}(z_1-z_2) \tag{B15}$$

which leads to

$$\begin{aligned}\Delta\gamma_2 &= -\frac{\pi}{2}\left(\frac{e}{mc^2}\right)^2\frac{K^2}{\lambda_u}\left(\frac{L}{\gamma}\right)^3\left(J_0(\xi)-J_1(\xi)\right)^2E_0^2\int_{-\frac{1}{2}}^{\frac{1}{2}}\int_{-\frac{1}{2}}^{z_1}\sin\left(q(z_1-z_2)\right)(z_1-z_2)dz_2\,dz_1 \\ &= -\frac{\pi}{2}\left(\frac{e}{mc^2}\right)^2\frac{K^2}{\lambda_u}\left(\frac{L}{\gamma}\right)^3\left(J_0(\xi)-J_1(\xi)\right)^2E_0^2\,f(q)\end{aligned} \tag{B16}$$

Here *f(q)* describes the detuning curve, i.e. the gain as a function of detuning. The actual average energy loss per electron is $\Delta\gamma_2\,mc^2$. Since the electron density per time-interval equals J/e, the total power density equals $P = \Delta\gamma_2\,mc^2\,J/e$. The power density, gained by the optical field thus becomes

$$P = \frac{\pi}{2}\frac{e}{mc^2}J\frac{K^2}{\lambda_u}\left(\frac{L}{\gamma}\right)^3\left(J_0(\xi)-J_1(\xi)\right)^2E_0^2\,f(q) \tag{B17}$$

The original average power density of the optical field equals $P_i = 4\pi\varepsilon_0\,c\,E_0^2/8\pi$. Hence the gain, $G = P/P_i$, equals

$$
\begin{aligned}
G &= 4\pi^2 \frac{1}{4\pi\varepsilon_0} \frac{e}{mc^3} J \frac{K^2}{\lambda_u} \left(\frac{L}{\gamma}\right)^3 \left(J_0(\xi) - J_1(\xi)\right)^2 f(q) \\
&= 4\pi^2 \frac{J}{I_A} \frac{K^2}{\gamma^3} \frac{L^3}{\lambda_u} \left(J_0(\xi) - J_1(\xi)\right)^2 f(q)
\end{aligned}
\tag{B18}
$$

with

$$
\begin{aligned}
f(q) &= \int_{-\frac{1}{2}}^{\frac{1}{2}} \int_{-\frac{1}{2}}^{z_1} \sin\left(q(z_1 - z_2)\right)(z_1 - z_2) dz_2 dz_1 \\
&= \frac{2 - 2\cos(q) - q\sin(q)}{q^3}
\end{aligned}
\tag{B19}
$$

B.2 Influence of finite energy spread

Due to a finite energy spread the phase of the electrons in the ponderomotive well will be disturbed. This phase disturbance can be described via the dispersion. Hence, the additional phase advance ϑ between z_1 and z_2 due to an energy deviation $\delta\gamma = (\gamma - \gamma_0)/\gamma_0$ can be written as

$$
\begin{aligned}
\vartheta(z_1, z_2, \delta\gamma) &= -\omega \Delta t(z_1, z_2, \delta\gamma) \\
&= -D(z_1, z_2)\, \delta\gamma
\end{aligned}
\tag{B20}
$$

When assuming a Gaussian energy distribution with variance σ_e for the electron beam:

$$
f_e = \frac{1}{\sigma_e \sqrt{2\pi}} \exp\left[-\frac{1}{2} \left(\frac{\delta\gamma}{\sigma_e}\right)^2 \right]
\tag{B21}
$$

the average influence of a finite energy spread can be calculated through a modification of *f(q)* to

$$
\begin{aligned}
f(q) &= \int_{-\infty}^{\infty} \int_{-\frac{1}{2}}^{\frac{1}{2}} \int_{-\frac{1}{2}}^{z_1} f_e(\delta\gamma) \Im\left\{\exp i\left[q(z_1 - z_2) + \vartheta(z_1, z_2, \delta\gamma)\right]\right\} D(z_1, z_2) dz_1 dz_2 d\gamma \\
&= \frac{1}{\sigma_e \sqrt{2\pi}} \int_{-\infty}^{\infty} \int_{-\frac{1}{2}}^{\frac{1}{2}} \int_{-\frac{1}{2}}^{z_1} \Im\left\{\exp i\left[q(z_1 - z_2)\right]\right\} \exp\left\{ -\frac{1}{2} \left(\frac{\delta\gamma}{\sigma_e}\right)^2 \right\} D(z_1, z_2) dz_1 dz_2 d\gamma \\
&= \frac{1}{\sigma_e \sqrt{2\pi}} \int_{-\infty}^{\infty} \int_{-\frac{1}{2}}^{\frac{1}{2}} \int_{-\frac{1}{2}}^{z_1} \Im\left\{\exp i\left[q(z_1 - z_2)\right]\right\} \\
&\qquad \exp\left\{ -\frac{1}{2} \left[\frac{\delta\gamma}{\sigma_e} - \sigma_e D(z_1, z_2) \right]^2 \right\} \exp\left\{ -\frac{1}{2} \left[\sigma_e D(z_1, z_2)\right]^2 \right\} D(z_1, z_2) dz_1 dz_2 d\gamma
\end{aligned}
$$

$$
f(q) = \int_{-\frac{1}{2}}^{\frac{1}{2}} \int_{-\frac{1}{2}}^{z_1} \Im\left\{\exp i\left[q(z_1 - z_2)\right]\right\} F_e(z_1, z_2) D(z_1, z_2) dz_1 dz_2
\tag{B22}
$$

with

$$F_e(z_1, z_2) = \exp\left\{ -\frac{1}{2}\left[\sigma_e D(z_1, z_2)\right]^2 \right\} \tag{B23}$$

B.3 Gain calculation for a real beam

In the following a Gaussian is assumed for both the distribution of the energy spread and the distribution in all directions in phase-space, i.e. $\delta\gamma$, x, x', y, and y'. Properties of the electron beam are defined through the variance of the energy-spread distribution, the β-functions, and the emittance, i.e. σ_e, ε_x, $\beta_x(z)$, ε_y, and $\beta_y(z)$. Hence, the distribution of the electron beam can be described as a 3D Gaussian function

$$\begin{aligned} f(\mathbf{X}) &= \sqrt{\frac{\det|\mathbf{A}|}{(2\pi)^5}} \exp\left(-\frac{1}{2}\mathbf{X}^T\mathbf{A}\mathbf{X} \right) \\ &= \frac{1}{\varepsilon_x \varepsilon_y \sigma_e} \frac{1}{(2\pi)^{5/2}} \exp\left(-\frac{1}{2}\mathbf{X}^T\mathbf{A}\mathbf{X} \right) \end{aligned} \tag{B24}$$

In a waist, i.e. at the centre of the undulator $\boldsymbol{A}$ can be expressed as

$$\mathbf{A}_{z=0} = \begin{pmatrix} \frac{1}{\beta_x\varepsilon_x} & 0 & 0 & 0 & 0 \\ 0 & \frac{\beta_x}{\varepsilon_x} & 0 & 0 & 0 \\ 0 & 0 & \frac{1}{\beta_y\varepsilon_y} & 0 & 0 \\ 0 & 0 & 0 & \frac{\beta_y}{\varepsilon_y} & 0 \\ 0 & 0 & 0 & 0 & \frac{1}{\sigma_e^2} \end{pmatrix} \quad \text{and} \quad \mathbf{X} = \begin{pmatrix} x \\ x' \\ y \\ y' \\ \delta\gamma \end{pmatrix} \tag{B25}$$

Assuming a linear transverse motion, both the evolution of the phase-space distribution can be described via the transport matrix $\boldsymbol{M}$ of the undulator. For a planar undulator this reads

$$\mathbf{M}(z) = \begin{pmatrix} 1 & z & 0 & 0 & 0 \\ 0 & 1 & 0 & 0 & 0 \\ 0 & 0 & \cos(z/\beta_{sc}) & \beta_{sc}\sin(z/\beta_{sc}) & 0 \\ 0 & 0 & -\frac{1}{\beta_{sc}}\sin(z/\beta_{sc}) & \cos(z/\beta_{sc}) & 0 \\ 0 & 0 & 0 & 0 & 1 \end{pmatrix} \tag{B26}$$

with $\beta_{sc} = \gamma/\mathrm{K}\, k_u = \gamma mc^2/eB$. Note that the focussing properties of the undulator are neglected. Gain reduction, due to a finite emittance and energy spread, can be calculated by averaging the electron motion with the phase-advance and intensity of the optical mode. For the latter a fundamental Gaussian (TEM_{00}) with Raleigh-length β_o will be assumed with a waist in the centre of the interaction region, i.e. $z = 0$. For this case Eq. (B1) expands to

$$E_x = \Re\left(E_0(z) e^{i(\omega t - kz - \varsigma(z,y,z) + \phi)} \right) \tag{B27}$$

$$\begin{aligned} E_0(z) &= \frac{E_0}{1 - i(z/\beta_o)} \\ \varsigma(z,y,z) &= \frac{k(x^2 + y^2)}{2(\beta_o - iz)} \end{aligned} \tag{B28}$$

Note that both x and y are functions of z, i.e. $x(z)$ and $y(z)$.

Similar as in Sec. B.2, *f(q)* will be modified to

$$f_X(q) = \int_{-\infty}^{\infty}\int_{-\frac{1}{2}}^{\frac{1}{2}}\int_{-\frac{1}{2}}^{z_1} \Im\left\{ \frac{1}{1-i(z_1/\beta_o)} \frac{1}{1+i(z_2/\beta_o)} \exp\left[\varsigma(\mathbf{X},z_1)+\varsigma^*(\mathbf{X},z_2)\right] \right.$$
$$\left. \exp i\left[q(z_1-z_2)+\vartheta(z_1,z_2,\mathbf{X})\right] \right\} f(\mathbf{X}) D(z_1,z_2)\, dz_1\, dz_2\, d\mathbf{X} \qquad \text{(B29)}$$

$$f_X(q) = \int_{-\frac{1}{2}}^{\frac{1}{2}}\int_{-\frac{1}{2}}^{z_1} \Im\left\{ \frac{1}{1-i(z_1/\beta_o)} \frac{1}{1+i(z_2/\beta_o)} e^{iq(z_1-z_2)}\, ff(z_1,z_2) \right\} D(z_1,z_2)\, dz_1\, dz_2$$

where $\vartheta(z_1,z_2,\mathbf{X})$ accounts for the additional phase advance of the electrons, either due to energy spread (see Sec. B.2), or due to transverse motion of the electrons. The latter can be expressed as

$$\vartheta(x',y,y',z_1,z_2) = -k(z_1-z_2)\left(x'^2 + y'^2 + \frac{y^2}{\beta_{sc}^2} \right) \qquad \text{(B30)}$$

The terms with x' and y' arise from the fact that an electron with transverse motion must have a reduced longitudinal motion. The dependence on y arises from the increased magnetic field strength as an electron moves closer to the poles of the undulator. Note that because of energy conservation the term $y'^2+(y/\beta_{sc})^2 = \text{const}$.

To simplify calculations averaging over the electron beam will be done in the centre of the undulator, i.e. $z = 0$. The beam parameters will be expanded according to the transport matrix $\boldsymbol{M}$. Equation (B28) therefore expands to

$$\varsigma(\mathbf{X},z) = \frac{1}{2}\frac{k}{\beta_o - iz}\left[(x+zx')^2 + \left(y\cos(z/\beta_{sc}) + \frac{y'}{\beta_{sc}}\sin(z/\beta_{sc}) \right)^2 \right] \qquad \text{(B31)}$$

and *ff* becomes

$$ff(z_1,z_2) = \sqrt{\frac{\det|\mathbf{A}|}{(2\pi)^5}} \int d\mathbf{X} \frac{1}{1-i(z_1/\beta_o)} \frac{1}{1+i(z_2/\beta_o)}$$
$$\exp -\frac{1}{2}\left[\frac{x^2}{\beta_x\varepsilon_x} + \frac{\beta_x x'^2}{\varepsilon_x} + \frac{k(x+z_1x')^2}{\beta_o - iz_1} + \frac{k(x+z_2x')^2}{\beta_o + iz_2} - ik(z_1-z_2)x'^2 \right]$$
$$\exp -\frac{1}{2}\left[\frac{y^2}{\beta_y\varepsilon_y} + \frac{\beta_y y'^2}{\varepsilon_y} + \frac{k\left(y\cos(z_1/\beta_{sc}) + y'\beta_{sc}\sin(z_1/\beta_{sc})\right)^2}{\beta_o - iz_1} \right.$$
$$\left. + [\ ] \frac{k\left(y\cos(z_2/\beta_{sc}) + y'\beta_{sc}\sin(z_2/\beta_{sc})\right)^2}{\beta_o + iz_2} - ik(z_1-z_2)\left(y'^2 + \frac{y^2}{\beta_{sc}^2} \right) \right]$$
$$\exp -\frac{1}{2}\left[\left(\frac{\delta\gamma}{\sigma_e} \right)^2 + 2D(z_1,z_2)\delta\gamma \right] \qquad \text{(B32)}$$

In a more general form the integral of $\mathbf{X}$ can be expressed as

$$ff(z_1,z_2)=\sqrt{\frac{\det|\mathbf{A}|}{(2\pi)^5}}\int\exp\left[-\frac{1}{2}\mathbf{X}^T\mathbf{W}(z_1,z_2)\mathbf{X}-\mathbf{V}^T(z_1,z_2)\mathbf{X}\right]d\mathbf{X} \qquad \text{(B33)}$$

In the equation the matrix **W** represents all terms with a squared dependence on **X**, e.g., *f(***X***)* and ϑ*(***X***,z)*. The vector **V** represents all terms that are linear with **X**, e.g. the influence of dispersion.

Similar to the approach used in Eq. (B22) a general solution for Eq. (B33) can be found through a linear transformation

$$\mathbf{Y}=\mathbf{X}+\mathbf{W}^{-1}(z_1,z_2)\mathbf{V}(z_1,z_2) \qquad \text{(B34)}$$

which transforms Eq. (B33) into

$$ff(z_1,z_2)=\sqrt{\frac{\det|\mathbf{A}|}{(2\pi)^5}}\int\exp\left[-\frac{1}{2}\mathbf{Y}^T\mathbf{W}(z_1,z_2)\mathbf{Y}+\mathbf{V}^T(z_1,z_2)\mathbf{W}(z_1,z_2)\mathbf{V}(z_1,z_2)\right]d\mathbf{X} \qquad \text{(B35)}$$

Because **W** is a symmetric matrix with its real part positive definite (all density distributions must be real and positive), Eq. (B35) can be integrated, leading to

$$ff(z_1,z_2)=\sqrt{\frac{\det|\mathbf{A}|}{(2\pi)^5}}\exp-\frac{1}{2}\left[\mathbf{V}^T(z_1,z_2)\mathbf{W}(z_1,z_2)\mathbf{V}(z_1,z_2)\right] \qquad \text{(B36)}$$

From Eq. (B32) it follows

$$\mathbf{W}(z_1,z_2)=\begin{pmatrix} w_{11} & w_{12} & 0 & 0 & 0\\ w_{12} & w_{22} & 0 & 0 & 0\\ 0 & 0 & w_{33} & w_{34} & 0\\ 0 & 0 & w_{34} & w_{44} & 0\\ 0 & 0 & 0 & 0 & w_{55}\end{pmatrix} \quad \text{and} \quad \mathbf{V}(z_1,z_2)=\begin{pmatrix} 0\\ 0\\ 0\\ 0\\ D(z_1,z_2)\end{pmatrix} \qquad \text{(B37)}$$

with

$$\begin{aligned}
w_{11}&=\frac{1}{\beta_x\varepsilon_x}+\frac{k}{\beta_o-iz_1}+\frac{k}{\beta_o+iz_2}\\
w_{12}&=\frac{kz_1}{\beta_o-iz_1}+\frac{kz_2}{\beta_o+iz_2}\\
w_{22}&=\frac{\beta_x}{\varepsilon_x}+\frac{kz_1^{\,2}}{\beta_o-iz_1}+\frac{kz_2^{\,2}}{\beta_o+iz_2}-ik(z_1-z_2)\\
w_{33}&=\frac{1}{\beta_y\varepsilon_y}+\frac{k\cos^2(z_1/\beta_{sc})}{\beta_o-iz_1}+\frac{k\cos^2(z_2/\beta_{sc})}{\beta_o+iz_2}-ik\frac{z_1-z_2}{\beta_{sc}^2}\\
w_{34}&=\frac{1}{2}\frac{k\sin(2z_1/\beta_{sc})}{\beta_o-iz_1}+\frac{1}{2}\frac{k\sin(2z_2/\beta_{sc})}{\beta_o+iz_2}\\
w_{44}&=\frac{\beta_y}{\varepsilon_y}+\frac{k\beta_{sc}^2\sin^2(z_1/\beta_{sc})}{\beta_o-iz_1}+\frac{k\beta_{sc}^2\sin^2(z_2/\beta_{sc})}{\beta_o+iz_2}-ik(z_1-z_2)\\
w_{55}&=\frac{1}{\sigma_e^2}
\end{aligned} \qquad \text{(B38)}$$

leading to $\det|\mathbf{W}| = \det|\mathbf{W}_x|\,\det|\mathbf{W}_y|\,\det|\mathbf{W}_e|$ with

$$\det|\mathbf{W}_x| = \frac{1}{\varepsilon_x^2}\left\{\left[1+k\varepsilon_x\beta_x\left(\frac{1}{\beta_o - iz_1}+\frac{1}{\beta_o+iz_2}\right)\right]\cdot \left[1+k\frac{\varepsilon_x}{\beta_x}\left(\frac{z_1^{\,2}}{\beta_o-iz_1}+\frac{z_2^{\,2}}{\beta_o+iz_2}-i(z_1-z_2)\right)\right] - \left[(k\varepsilon_x)^2\left(\frac{z_1}{\beta_o-iz_1}+\frac{z_2}{\beta_o+iz_2}\right)^2\right]\right\}$$

$$\det|\mathbf{W}_y| = \frac{1}{\varepsilon_y^2}\left\{\left[1+k\varepsilon_y\beta_y\left(\frac{\cos^2(z_1/\beta_{sc})}{\beta_o-iz_1}+\frac{\cos^2(z_2/\beta_{sc})}{\beta_o+iz_2}-i\frac{z_1-z_2}{\beta_{sc}^2}\right)\right]\cdot \left[1+k\frac{\varepsilon_y}{\beta_y}\left(\frac{\beta_{sc}^2\sin^2(z_1/\beta_{sc})}{\beta_o-iz_1}+\frac{\beta_{sc}^2\sin^2(z_2/\beta_{sc})}{\beta_o+iz_2}-i(z_1-z_2)\right)\right] - \left[\left(\frac{k\varepsilon_y}{2}\right)^2\left(\frac{\sin(2z_1/\beta_{sc})}{\beta_o-iz_1}+\frac{\sin(2z_2/\beta_{sc})}{\beta_o+iz_2}\right)^2\right]\right\}$$

$$\det|\mathbf{W}_e| = \frac{1}{\sigma_e^2} \tag{B39}$$

and

$$\exp-\frac{1}{2}\left[\mathbf{V}^T\mathbf{W}\mathbf{V}\right] = \exp-\frac{1}{2}(\sigma_e D)^2 \tag{B40}$$

identical to F_e in Eq. (B23). Hence $f(q)$ can be written as (see Eq. (B29))

$$f = \int_{-\frac{1}{2}}^{\frac{1}{2}}\int_{-\frac{1}{2}}^{z_1}\Im\left\{\frac{1}{1-i(z_1/\beta_o)}\frac{1}{1+i(z_2/\beta_o)} F_x(z_1,z_2)F_y(z_1,z_2)F_e(z_1,z_2)e^{iq(z_1-z_2)}\right\}(z_1-z_2)dz_1dz_2 \tag{B41}$$

which leads to a gain of

$$G = 8\pi^2\frac{I}{I_A}\frac{K^2}{\gamma^3}\frac{L^3}{\lambda_u\lambda\beta_o}\left(J_0(\xi)-J_1(\xi)\right)^2 \int_{-\frac{1}{2}}^{\frac{1}{2}}\int_{-\frac{1}{2}}^{z_1}\Im\left\{\frac{1}{1-i(z_1/\beta_o)}\frac{1}{1+i(z_2/\beta_o)} F_x(z_1,z_2)F_y(z_1,z_2)F_e(z_1,z_2)e^{iq(z_1-z_2)}\right\}(z_1-z_2)dz_1dz_2 \tag{B42}$$

Here J has been substituted for the peak current I divided by the mode area of the electric field:

$$\Sigma_A = \frac{\lambda\beta_o}{2} \tag{B43}$$

and F is given by

$$F_x = \left\{\left[1 + k\varepsilon_x\beta_x\left(\frac{1}{\beta_o - iz_1} + \frac{1}{\beta_o + iz_2}\right)\right]\cdot\left[1 + k\frac{\varepsilon_x}{\beta_x}\left(\frac{{z_1}^2}{\beta_o - iz_1} + \frac{{z_2}^2}{\beta_o + iz_2} - i(z_1 - z_2)\right)\right]\right.$$
$$\left.-\left[(k\varepsilon_x)^2\left(\frac{z_1}{\beta_o - iz_1} + \frac{z_2}{\beta_o + iz_2}\right)^2\right]\right\}^{-\frac{1}{2}}$$

$$F_y = \left\{\left[1 + k\varepsilon_y\beta_y\left(\frac{\cos^2(z_1/\beta_{sc})}{\beta_o - iz_1} + \frac{\cos^2(z_2/\beta_{sc})}{\beta_o + iz_2} - i\frac{z_1 - z_2}{\beta_{sc}^2}\right)\right]\cdot\right.$$
$$\left[1 + k\frac{\varepsilon_y}{\beta_y}\left(\frac{\beta_{sc}^2\sin^2(z_1/\beta_{sc})}{\beta_o - iz_1} + \frac{\beta_{sc}^2\sin^2(z_2/\beta_{sc})}{\beta_o + iz_2} - i(z_1 - z_2)\right)\right]$$
$$\left.-\left[\left(\frac{k\varepsilon_y}{2}\right)^2\left(\frac{\sin(2z_1/\beta_{sc})}{\beta_o - iz_1} + \frac{\sin(2z_2/\beta_{sc})}{\beta_o + iz_2}\right)^2\right]\right\}^{-\frac{1}{2}}$$

$$F_e = \exp -\frac{1}{2}(\sigma_e D)^2 \tag{B44}$$

B.4 The optical klystron

For the OK the assumption is made that the interaction between the electrons and the optical wave can be neglected within the drift section of the OK which thus becomes a linear combination of two undulators, separated by a drift section. Now the symmetric OK will be investigated, i.e. the drift section occupies a system with a total length L where the centre part L_d. In the drift section the optical wave-front advances N_d wavelengths, relative to the electron beam. A drift length $(z_1\text{-}z_2)$ thus modifies to

$$\Delta z = z_1 - z_2 \mapsto \begin{cases} z_1 + N_d/N - z_2, & z_1 \geq \frac{1}{2}L_d \wedge z_2 \leq -\frac{1}{2}L_d \\ z_1 - z_2 & \text{other} \end{cases} \tag{B45}$$

and the gain becomes

$$G = 8\pi^2\frac{I}{I_A}\frac{K^2}{\gamma^3}\frac{N^3\lambda_u^2}{\lambda\beta_o}\left(J_0(\xi) - J_1(\xi)\right)^2$$
$$\int_{-\frac{1}{2}}^{\frac{1}{2}}\int_{-\frac{1}{2}}^{z_1}\Im\left\{\frac{1}{1 - i(z_1/\beta_o)}\frac{1}{1 + i(z_2/\beta_o)}\right.$$
$$\left.g(z_1)g(z_2)F_x(z_1, z_2)F_y(z_1, z_2)F_e(z_1, z_2)e^{iq\Delta z}\right\}\Delta z dz_1 dz_2 \tag{B46}$$

$$g(z) = \begin{cases} 0, & |z| < L_d/2L \\ 1, & |z| \geq L_d/2L \end{cases}$$

where $g(z)$ arises from the fact that the interaction in the drift space of the OK is neglected. Note that N is the total number of undulator periods (divided over two undulators).